The complex diagenetic history of discontinuities in shallow- marine carbonate rocks: New insights from high-resolution ion microprobe investigation of d 18 O and d 13 C of early cements

Simon Andrieu, Benjamin Brigaud, Jocelyn Barbarand, Eric Lasseur

Sedimentology (2017) doi: 10.1111/sed.12384

The complex diagenetic history of discontinuities in shallow-marine carbonate rocks: New insights from high-resolution ion microprobe investigation of $\delta^{18}O$ and $\delta^{13}C$ of early cements

SIMON ANDRIEU*, BENJAMIN BRIGAUD*, JOCELYN BARBARAND* and ERIC LASSEUR†
*GEOPS, Univ. Paris-Sud, CNRS, Université Paris Saclay, Rue du Belvédère, Bât. 504, 91405 Orsay, France (E-mail: simon.andrieu@u-psud.f)
†BRGM, 3 avenue Claude Guillemin, BP 36009, 45060 Orléans, France

Associate Editor – Christian Betzler

ABSTRACT

Sedimentary gaps are a major obstacle in the reconstruction of a carbonate platform's history. In order to improve the understanding of the early diagenesis and the succession of events occurring during the formation of discontinuity surfaces in limestones, secondary ion mass spectrometry was used for the first time to measure the $\delta^{18}O$ and $\delta^{13}C$ signatures of 11 early cement and fabric stages in several discontinuity surfaces from the Jurassic carbonate platform of the Paris Basin, France. Pendant cements show a high variability in $\delta^{18}O$, which was impossible to detect by the less precise microdrilling method. The morphology of a given cement can be produced in various environments, and dogtooth cements especially can precipitate in marine phreatic and meteoric phreatic to vadose environments. Marine dogtooth cements and micritic microbially induced fabrics precipitated directly as low-magnesium calcite in marine waters, as attested to by the preservation of their initial $\delta^{18}O$ and $\delta^{13}C$ signals. Five discontinuity types are recognized based on high-resolution geochemical analyses, and their palaeoenvironmental history can be reconstructed. Two exposure surfaces with non-ferroan pendant or meniscus cements formed in the oxidizing vadose zone. A hardground displays marine fibrous cements and non-ferroan dogtooth cements that formed in a subtidal environment in oxidizing water. Two composite surfaces have undergone both marine and subaerial lithification. Composite surface 1 displays non-luminescent ferroan dogtooth cements that precipitated in reduced conditions in seawater, followed by brown-luminescent dogtooth cements characteristic of a meteoric phreatic environment. Composite surface 2 exhibits microbially induced fabrics that formed in marine water with abundant organic matter. The latter discontinuity, initially formed in a subtidal environment, was subsequently exposed to meteoric conditions, as evidenced by ferroan geopetal cements. A high-resolution ion microprobe study is essential to precisely document the successive diagenetic environments that have affected carbonate rocks and discontinuities with a polygenic and intricate history.

Keywords Carbonate, diagenesis, discontinuities, early cements, oxygen and carbon isotopes, SIMS.

INTRODUCTION

Discontinuities are key horizons in the marine sedimentary record related to a break in sedimentation or *hiatus* (Bathurst, 1975; Clari *et al.*, 1995; Immenhauser *et al.*, 2000); they display wide variability in carbonate rocks as they may form in submarine environments or during subaerial exposure, which can be intermittent or prolonged (Hillgärtner, 1998; Sattler *et al.*, 2005; Martinuš *et al.*, 2012). These surfaces are used as marker horizons for correlating stratigraphic sections at basin scale and beyond (Kauffman *et al.*, 1991; Immenhauser *et al.*, 2000; Christ *et al.*, 2015), and as depositional unit boundaries in sequence stratigraphy (Durlet & Loreau, 1996; Loreau & Durlet, 1999; Christ *et al.*, 2012a, b, 2015; Vincent *et al.*, 2015). Discontinuities generally have multiphase histories, because they sometimes record several successive phases of regression and transgression (Hamon *et al.*, 2005), and it is essential to combine both geochemical and petrographic techniques in order to decipher their complex formation (Videtich & Matthews, 1980). All of the chemical, physical and biochemical transformations that occur when the water chemistry is controlled by the depositional environment are referred to as early diagenesis or eogenesis (Pagel *et al.*, 2014). The morphology and chemical properties of early cements reflect the changes in environmental conditions (pore water type, redox conditions, alkalinity and pH) during sedimentary *hiatuses* (Purser, 1969; Loreau & Durlet, 1999; Flügel, 2010; Christ *et al.*, 2012a,b, 2015). These cements are a key tool for tracing the origins and history of discontinuities (Durlet & Loreau, 1996; Loreau & Durlet, 1999).

However, it is highly unlikely to be able to unequivocally decipher the origins of early cements from their morphology alone, as the latter may refer to a formation in different settings (Flügel, 2010; Christ *et al.*, 2015; Godet *et al.*, 2016). The nature of some early cements has been misinterpreted before. As an example, micritic meniscus cements (meniscus-like cements) were considered to be sure indicators of vadose diagenesis until Hillgärtner *et al.* (2001) demonstrated that they may also form in subtidal environments.

The origins of early cements can be more reliably defined from their $\delta^{18}O$ and $\delta^{13}C$ signatures that are, together with their petrography, used to constrain the type of water (meteoric or marine) from which they precipitated and to reveal the possible organic-matter influence leading to their enrichment in ^{12}C (Godet *et al.*, 2016). Moreover, carbon and oxygen stable isotope geochemistry may also allow for the determination of the initial mineralogy of early cements. While some authors claim that marine micrite precipitated in aragonite and high-magnesium calcite throughout the Phanerozoic (Folk, 1974; Bates & Brand, 1990), recent studies suggest that low-magnesium micrite can form during calcite sea periods (Volery *et al.*, 2009, 2010a,b, 2011; Turpin *et al.*, 2014).

Microdrilling is commonly used to obtain the isotopic composition of blocky calcite or millimetre-sized to centimetre-sized non-recrystallized shells. However, it is far less adapted to precisely sample early cements that are less than few tens of micrometres wide. Moreover, because of the low accuracy of microdrilling, $\delta^{18}C$ and $\delta^{13}C$ results could reflect mixing with later burial overgrowths and cements. Oxygen and carbon isotope signatures have already been acquired for well-developed early cements such as microbially generated fabrics, botryoidal cements (Christ *et al.*, 2012a), radiaxial and fascicular fibrous cements (Tobin *et al.*, 1996; Christ *et al.*, 2012a; Dickson & Kenter, 2014), pendant cements (Ronchi *et al.*, 2010; Brigaud *et al.*, 2014b; Dickson & Kenter, 2014) and scalenohedral cements (Godet *et al.*, 2016). However, such measurements are limited to exceptionally well-developed early cements; they do not reflect all the variability of cement types, especially since similar morphologies may have different geochemical compositions and, above all, they do not inform on the intra-cement variability. Indeed, one cement can initially form in a diagenetic environment and continue to precipitate in another environment while still exhibiting optical continuity.

Investigative size is thus an obstacle for many diagenetic studies, especially on early cements, which are generally <50 μm in size. Not having access to the isotopic composition and variability of these small cement crystals strongly limits current understanding of the physical and chemical processes involved in early diagenesis, and the subsequent formation of discontinuities.

In this study, the $\delta^{18}O$ and $\delta^{13}C$ values of diagenetic products were measured directly on thin sections by secondary ion mass spectrometry (SIMS) using the IMS-1280 (Cameca, Gennevilliers Cedex, France). This equipment enables high-resolution investigation, with an analysis spot diameter of 20 μm. This technique has already been used occasionally for sedimentological studies (Rollion-Bard *et al.*, 2003, 2008;

Allison *et al.*, 2007; Cox *et al.*, 2010). Durlet & Loreau (1996) and Loreau & Durlet (1999) applied such measurements to analyse scalenohedral banded cements.

The Middle Jurassic and Oxfordian carbonate series of the Paris Basin display a broad spectrum of various early cements (meniscus, pendant, fibrous, dogtooth, meniscus-like cements and micritic envelopes) distributed within discontinuities such as subaerial unconformities or marine hardgrounds (Brigaud *et al.*, 2009b; Carpentier *et al.*, 2014) and provide an ideal case study where the origin of early cements and fabrics, and their mineralogical and chemical changes, can be assessed at a high-resolution scale.

The main objective of this study was to identify and understand high-resolution changes in palaeoenvironmental conditions (pore water characteristics, redox conditions, presence of organic matter and microbial influence) during the formation of discontinuities by measuring the $\delta^{18}O$ and $\delta^{13}C$ values of early cements. Subordinate objectives are as follows: (i) to determine the original mineralogy of early cements formed during the Jurassic with a special focus on the micritic cements; and (ii) to be more predictive about the types of environments in which a same cement morphology can form.

GEOLOGICAL SETTING AND SAMPLES

Eight samples at three sites in the Paris Basin (Andrieu *et al.*, 2016) were selected at and beneath six discontinuity surfaces, five of which correspond to third-order sequence boundaries. The Paris Basin is an intracontinental sedimentary basin filled with Triassic to Quaternary deposits overlying a Cadomian and Variscan basement (Fig. 1A; Guillocheau *et al.*, 2000). The carbonate rocks in this study are dated as Middle and Late Jurassic in age, a time when the Paris Basin was located at subtropical latitudes (20 to 30°N) and was covered by a shallow epicontinental sea connected to the Atlantic, Tethys and Arctic oceans (Fig. 1B and C; Enay & Mangold, 1980; Thierry & Barrier, 2000). Sites 1 and 2 are in the western Paris Basin, south of Caen and Alençon, respectively. Three carbonate samples collected from outcrop at Site 1 were studied: FAY11, VSH6 and VSH10. The FAY11 sample comes from the top of the Sables et Graviers de Tessé Formation (discontinuity Bj1, Fay quarry) dated as late Aalenian (*Concavum* zone) in age by the ammonites *Graphoceras* sp. and *Graphoceras cornu* (Fig. 1D). The samples VSH6 and VSH10 were collected from the lower part of the Calcaire corallien Mortagne Formation, dated as Mid Oxfordian by its brachiopod fauna, below and above discontinuity Ox1 (Moguedet *et al.*, 1998; Vouvray-sur-Huisne quarry; Fig. 1D). Two carbonate samples from Site 2 were studied: AU4 and LION5. Sample AU4 was collected from the mid-Bathonian Calcaire de Blainville (determined by the presence of ammonite and brachiopod fauna of the *Morrisi* zone; Rioult *et al.*, 1989; les Aucrais quarry), below discontinuity Bt2. Sample LION5 was collected from the late Bathonian Calcaire de Ranville Formation, dated by the presence of brachiopod fauna in the *Discus* zone (Rioult *et al.*, 1989; Lion-sur-mer cliffs), below discontinuity Bt4. Finally, samples E409, E427 and E436 come from borehole EST433 drilled by Andra (French National Radioactive Waste Management, Agency; study area 3) in the eastern part of the basin and were collected, respectively, from the Oolithe de Fréville Formation, below discontinuity Bt4 (late Bathonian *Discus* zone; Brigaud *et al.*, 2009a); from the Calcaire de Chaumont Formation, below discontinuity Bt3 (late Bathonian *Hodsoni* zone; Brigaud *et al.*, 2009a); and from the Calcaires de Chaumont Formation, below discontinuity Bt2 (mid-Bathonian *Morrisi* zone, Brigaud *et al.*, 2009a).

MATERIAL AND METHODS

Thin sections were made from the eight samples, and epoxy resin (polyepoxide) was used for the induration of the carbonate rocks. Thin sections were studied by optical microscopy with alizarin–potassium ferricyanide staining and by cathodoluminescence (CL) microscopy to characterize cement paragenesis. The CL analyses were carried out using a Cathodyne cold-cathode luminescence apparatus (OPEA, Fontenay-sous-Bois, France), operating at 14 kV and 150 to 250 μA, and coupled to an Olympus BX41 microscope (Olympus Corporation, Tokyo, Japan). Cement stratigraphy and diagenetic sequencing were established on the basis of geometrical relationships (superposition or cross-cutting). Major element compositions (Ca, Fe, Mg, Mn and Sr) of calcite were analysed on six carbon coated thin sections (FAY11, VSH6, VSH10, AU4, E409 and E436) using the SXFive electron probe micro analyser (EMPA; Cameca, Gennevilliers Cedex, France) at the Centre Camparis (Université Pierre

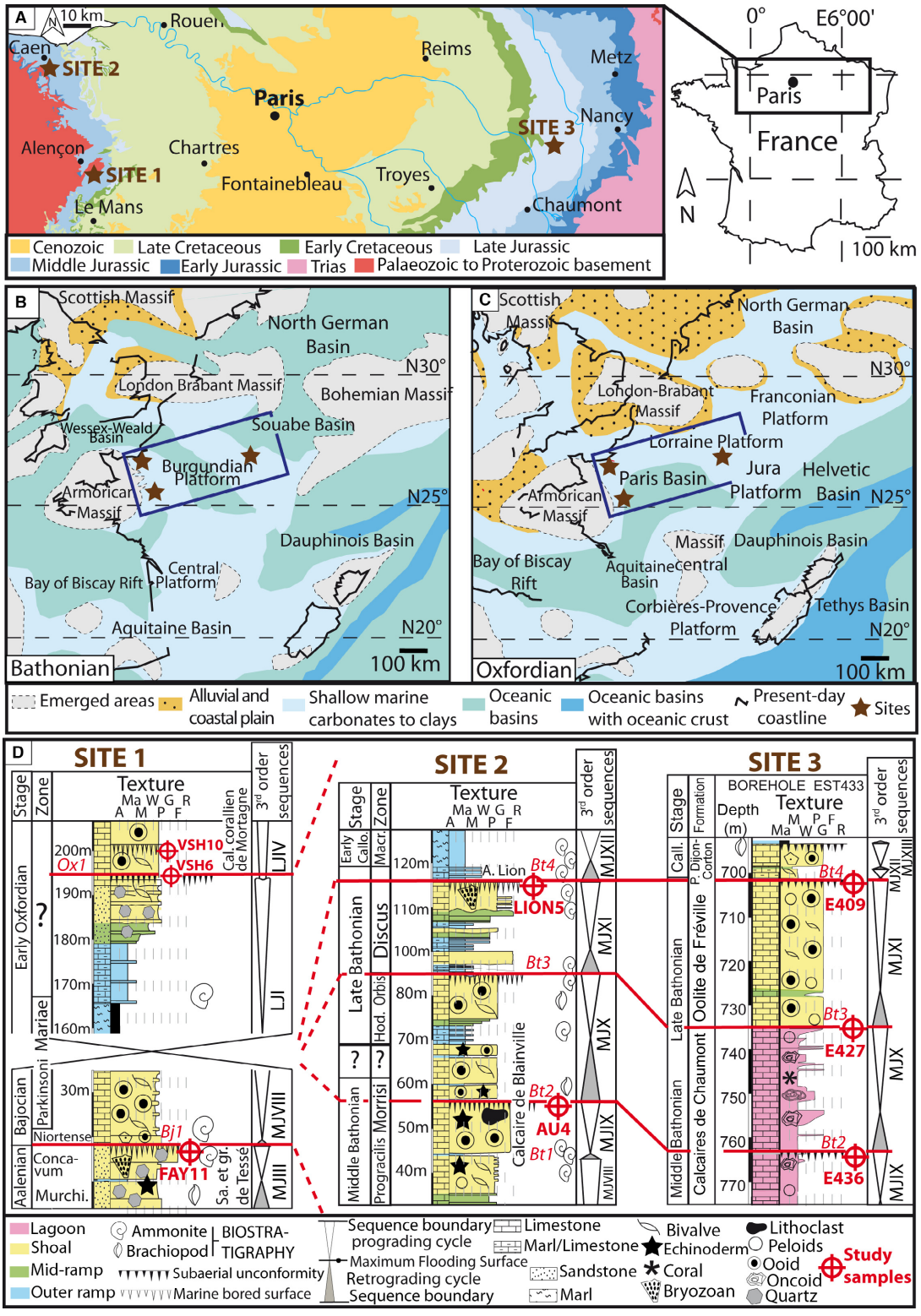

Fig. 1. (A) Study area locations on a geological map of the Paris Basin (France). (B) Location of the study area during the Bathonian in a palaeogeographic reconstruction (modified from Brigaud *et al.*, 2009a; based on Enay & Mangold, 1980; Ziegler, 1988; Thierry & Barrier, 2000; Hendry, 2002). (C) Location of the study area during the Oxfordian in a palaeogeographic reconstruction (modified from Strasser *et al.*, 2015; based on Enay & Mangold, 1980; Ziegler, 1988; Thierry & Barrier, 2000). (D) Location of the study samples on the stratigraphic log of the study areas in a biostratigraphic and sequence stratigraphic framework. The log of Site 3 is modified from Brigaud *et al.* (2009a).

et Marie Curie, Paris, France). The primary ion beam diameter was approximately 10 μm. Calibration standards used were pyroxene (Phn9) for magnesium and calcium, hematite (Fe_2O_3) for iron, volcanic glass for strontium (SrSi) and manganese titanate for the manganese (Mnti). Compositions of Ca, Mg, Mn, Fe and Sr are expressed as molar percentages (%) of $CaCO_3$, $FeCO_3$, $MgCO_3$, $MnCO_3$ and $SrCO_3$ in calcite. Measurement accuracy was on the order of 1·3% for the $CaCO_3$ (from 1·2% to 1·4%) and 0·01% for $MgCO_3$, $MnCO_3$, $FeCO_3$ and $SrCO_3$ (from 0·007% to 0·03%).

The *in situ* analyses were made using secondary ion mass spectrometry (SIMS) on polished thin sections using the IMS-1280 (CAMECA) at the Centre de Recherches Pétrographiques et Géochimiques (CRPG) in Nancy, France. Six thin sections (FAY11, VSH6, VSH10, AU4, E409 and E436) were cut to be adapted to the apparatus (30 mm long and 23 mm wide rectangles) and coated with gold before analysis. The primary ion beam diameter varied from 20 μm for oxygen isotope measurements to 10 μm for carbon isotope measurements, and the depth of the crater resulting from ablation was <1 μm. Measurement accuracy was of the order of 0·15‰ for oxygen isotopes (0·1 to 0·2‰ depending on the analysis) and 0·6‰ for carbon isotope (0·2 to 1·2‰). The calibration standard used was a calcite crystal (Carb4) with a $\delta^{18}O$ value of 11·26‰ SMOW (Standard Mean Ocean Water) and a $\delta^{13}C$ value of −5·46‰ PDB (Pee Dee Belemnite). For a complete description of the material and protocol, refer to Rollion-Bard *et al.* (2007). All results are presented in per mil deviation from the PDB standard (‰ PDB). The conversion from $\delta^{18}O$ SMOW to $\delta^{18}O$ PDB was made using the equation of Morse & Mackenzie (1990); $\delta^{18}O_{SMOW} = 1{\cdot}03086 \times \delta^{18}O_{PDB} + 30{\cdot}86$.

In total, 138 coupled $\delta^{13}C$ and $\delta^{18}O$ measurements were performed at distances of approximately 10 μm along ten transects: two transects on thin-section AU4, one on thin-section VSH10, three on thin-section VSH6, one on thin-section E436, one on thin-section E409 and two on thin-section FAY11. Ten other $\delta^{18}O$ measurements are not associated with $\delta^{13}C$, as early cements were too small to allow two analyses side by side.

RESULTS

Sixteen diagenetic events (13 early cement and fabric stages, a dissolution stage, a burial cementation stage and a telogenetic cementation stage) were identified and ordered in a paragenetic sequence (Fig. 2): (i) micritic envelopes; (ii) meniscus-like cements (*sensu* Hillgärtner *et al.*, 2001); (iii) micritization; (iv) geopetal peloidal fabrics; (v) isopachous fibrous cements; (vi) dissolution of aragonite shells; (vii) pendant cements; (viii) microsparitic bridge cements; (ix) meniscus cements; (x) non-isopachous dogtooth cements; (xi) non-ferroan dogtooth to syntaxial cements; (xii) ferroan dogtooth to syntaxial cements; (xiii) microsparitic ferroan geopetal cements; (xiv) brown-luminescent banded dogtooth cements; (xv) blocky calcites; and (xvi) microsparitic non-ferroan geopetal cements. These diagenetic stages are listed in Table 1 and include general characteristics (morphology and size), original mineralogy, CL, colours of the alizarin–potassium ferricyanide stained cements, geochemical properties ($\delta^{18}O$, $\delta^{13}C$, molar percentages of $FeCO_3$, $MnCO_3$, $MgCO_3$ and $SrCO_3$) and environment of formation.

Petrography of discontinuities

Diagenetic stages are located on the stratigraphic logs below the different discontinuities shown in Fig. 3, using the diagenetic log graphic visualization adapted from Durlet *et al.* (1992). Five discontinuities among the six studied correspond to third-order sequence boundaries (Brigaud *et al.*, 2014a,b; Andrieu *et al.*, 2016; Fig. 3). According to the sequence stratigraphy definition of Catuneanu *et al.* (2011), the discontinuities studied correspond either to a subaerial unconformity (SU) for Bt2 at sites 2 and 3, Bt4 at Site 3 (Brigaud *et al.*, 2014b) and Ox1 at Site 1 (Andrieu *et al.*, 2016), or to a marine maximum regressive surface for Bj1 at Site 1 and Bt3 at Site 2 (MRS; Andrieu *et al.*, 2016; Fig. 3).

Micritic envelopes are found below all of the studied discontinuities although they are mostly developed below surface Bt2 (sample AU4; Fig. 3). Micritic envelopes formed before the dissolution of aragonitic shells, which was the second diagenetic event found for all studied samples.

Discontinuity Bj1 (Aalenian/Bajocian transition) corresponds to a perforated hardground encrusted by bivalves (Figs 3 and 4A). The underlying sediments display well-developed isopachous fibrous cements that are followed by non-luminescent and non-ferroan dogtooth cements (Figs 3 and 4B). Around echinoderms, an early stage of non-luminescent and non-

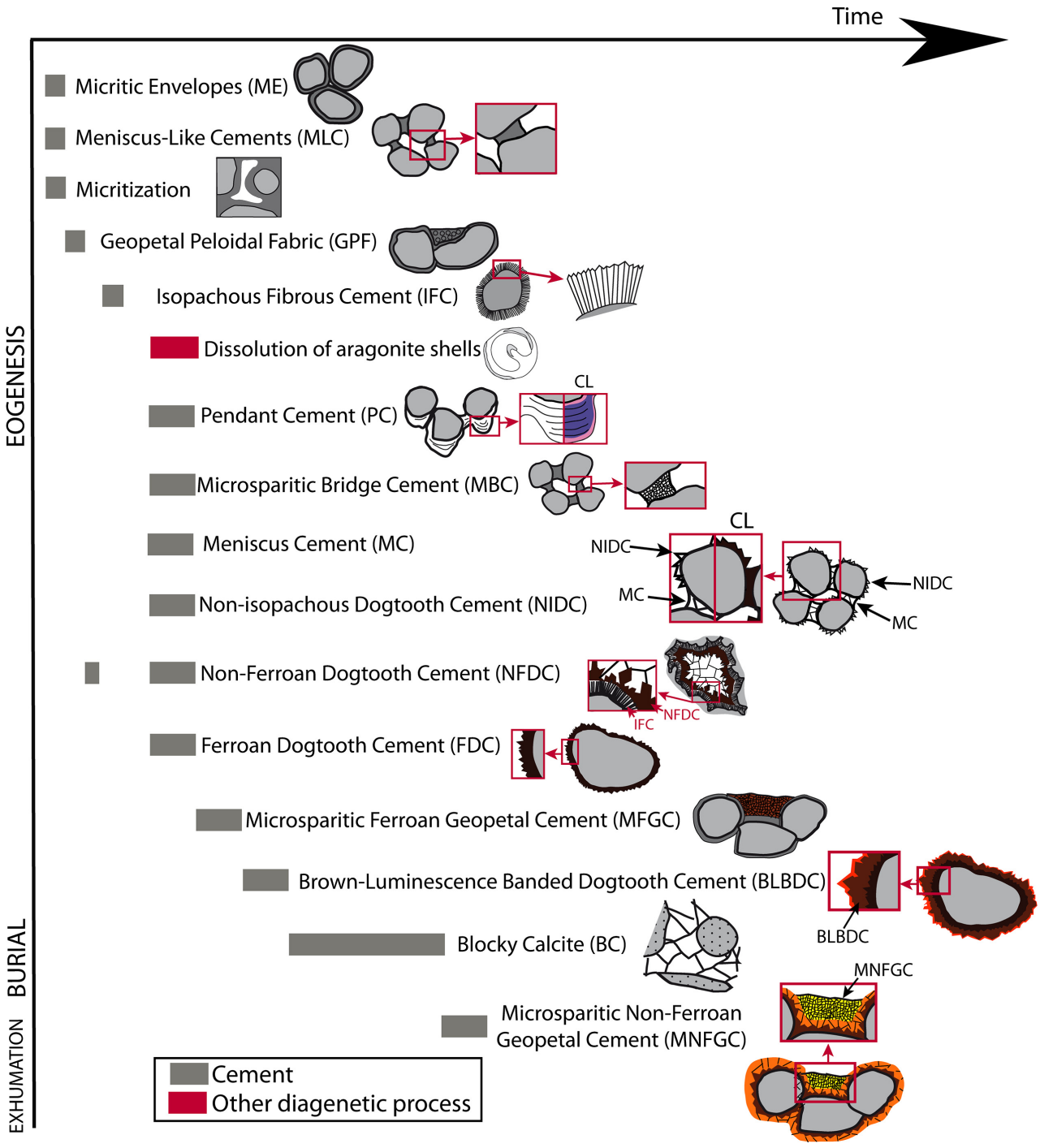

Fig. 2. Simplified paragenetic sequence of the Middle Jurassic and Oxfordian carbonate of the Paris Basin. The diagenetic stages are composed of micritic envelopes (ME), meniscus-like cements (MLC; *sensu* Hillgärtner, *et al.* 2001), micritization, geopetal peloidal fabric (GPF), isopachous fibrous cements (IFC), dissolution of aragonite shells, pendant cements (PC), microsparitic bridge cements (MBC), meniscus cements (MC), non-isopachous dogtooth cements (NIDC), non-ferroan dogtooth to syntaxial cements (NFDC), ferroan dogtooth to syntaxial cements (FDC), microsparitic ferroan geopetal cements (MFGC), brown-luminescent banded dogtooth cements (BLBDC), blocky calcite cementation (BC) and microsparitic non-ferroan geopetal cements (MNFGC).

Table 1. General characteristics, original mineralogy, cathodoluminescence and alizarin–potassium ferricyanide staining, geochemical properties and environments of formation of the different early cements and fabrics studied.

Cement/grain types	General characteristics	Original mineralogy	Cathodoluminescence	Alizarin/ ferricyanide	Major elements (median value)	Carbon and oxygen stable isotopes	Environment of formation
Non-bioclastic grains	Ooids and lithoclasts: micrite	Aragonite and/or high-Mg calcite	Orange to dark brown luminescence	–	–	$\delta^{18}O$: −10·8‰ to −3·7‰ *median value: −36‰* $\delta^{13}C$: −23‰ to 0·4‰ *median value: 11·9‰*	Micritic grains recrystallized in low-Mg calcite during burial
Recrystallized bioclastic grains	Echinoderms and recrystallized bivalves	Aragonite and/or high-Mg calcite	Orange to dark brown luminescence	–	–	$\delta^{18}O$: −5·3‰ to −2·6‰ *median value: −3·9‰* $\delta^{13}C$: −6·6‰ to 0·7 ‰ *median value: −0·7‰*	Bioclasts recrystallized in low-Mg calcite during burial
Micritic envelopes (ME)	Micritic envelopes around grains (50 to 100 μm)	Low-Mg calcite	Orange luminescence	Pink stained, non-ferroan calcite	$FeCO_3$: 0·88 mol%; $MnCO_3$: 0·11 mol%, $MgCO_3$: 0·01 mol%; $SrCO_3$: 0·04 mol%	$\delta^{18}O$: −1·4‰ to −1‰ *median value: −1·2‰* $\delta^{13}C$: −20‰ to −3·4‰ *median value: −11·7‰*	Microbial origin Subtidal *Marine phreatic*
Meniscus-like cements (MLC)	Micritic meniscus cements (200 to 500 μm)	Low-Mg calcite	Orange luminescence	Pink stained, non-ferroan calcite	$FeCO_3$: 0·15 mol%; $MnCO_3$: 0·02 mol%, $MgCO_3$: 1·28 mol%; $SrCO_3$: 0·04 mol%	$\delta^{18}O$: −2·5‰ to −1·1‰ *median value: −1,8‰* $\delta^{13}C$: −17·8‰ to −0·1 ‰ *median value: −12‰*	Microbial origin Subtidal *Marine phreatic*
Micritization	Micrite filling intergranular space	–	Bright orange luminescence	Pink stained, non-ferroan calcite	–		Subtidal to intertidal *Marine phreatic*
Geopetal peloidal fabrics (GPF)	Geopetal peloidal fabric (200 to 500 μm)	Low-Mg calcite	Orange luminescence	Pink stained, non-ferroan calcite	$FeCO_3$: 0·22 mol%; $MnCO_3$: 0·02 mol%, $MgCO_3$: 1·27 mol%; $SrCO_3$: 0·04 mol%	$\delta^{18}O$: −2·4‰ $\delta^{13}C$: −15‰	Subtidal to intertidal *Marine phreatic*
Isopachous fibrous cements (IFC)	Fibrous crystals – 50 to 100 μm	Aragonite and/or high-Mg calcite	Turbid luminescence (cloudy brown to yellow)	Blue stained, ferroan calcite	$FeCO_3$: 0·55 mol%; $MnCO_3$: 0·25 mol%, $MgCO_3$: 0·56 mol%; $SrCO_3$: 0·02 mol%	$\delta^{18}O$: −6‰ to −3‰ *median value: −5‰* $\delta^{13}C$: −0·1‰ to −6·1‰ *median value: −1·3‰*	Shallow marine (hardground) *Marine phreatic*
Pendant cements (PC)	Asymmetrical crusts of laminated layers – several millimetres thick	Low-Mg calcite	Dark-blue luminescence with pink brightly luminescent bands	Pink stained, non-ferroan calcite	$FeCO_3$: 0 mol%; $MnCO_3$: 0 mol%, $MgCO_3$: 2·07 mol%; $SrCO_3$: 0·06 mol%	$\delta^{18}O$: −6·6‰ to −1·9‰ *median value: −4·1‰* $\delta^{13}C$: −1·1‰ to 4·9‰ *median value: 0·8‰*	Intertidal to supratidal (no soil horizon) *Meteoric vadose*

Table 1. (continued)

Cement/grain types	General characteristics	Original mineralogy	Cathodoluminescence	Alizarin/ferricyanide	Major elements (median value)	Carbon and oxygen stable isotopes	Environment of formation
Microsparitic bridge cements (MBC)	Non-isopachous microsparitic cements forming a bridge between grains (100 μm to 1 mm)	Low-Mg calcite	Non-luminescent	Blue stained, ferroan calcite	$FeCO_3$: 0·21 mol%; $MnCO_3$: 0·02 mol%, $MgCO_3$: 1·25 mol%; $SrCO_3$: 0·02 mol%	$\delta^{18}O$: −4·1‰ to 0‰ *median value: −1·7‰* $\delta^{13}C$: −0·9‰ to 4·2‰ *median value: 1·7‰*	Subtidal to intertidal *Marine to mixed water, phreatic*
Meniscus cements (MC)	Asymmetrical cements between grains (100 μm to 200 μm, MC)	Low-Mg calcite	Non-luminescent	Pink stained, non-ferroan calcite	$FeCO_3$: 0·02 mol%; $MnCO_3$: 0 mol%, $MgCO_3$: 0·81 mol%; $SrCO_3$: 0·03 mol%	$\delta^{18}O$: −5·5‰ to −3·7‰ *median value: −4·3‰* $\delta^{13}C$: −14·8‰ to 4·4‰ *median value: −5·5‰*	Supratidal to continental with soil horizon *Meteoric vadose*
Non-isopachous dogtooth cement (NIDC)	Asymmetrical cements between grains (100 to 200 μm, MC) and dogtooth cements that do not form an isopachous fringe around grains (10 to 20 μm, ADC)	Low-Mg calcite	Non-luminescent	Pink stained, non-ferroan calcite	–	–	Supratidal to continental with soil horizon *Meteoric vadose*
Non-ferroan dogtooth cements (NFDC) to syntaxial cements	Dogtooth fringes (20 to 200 μm); syntaxial calcite overgrowth around echinoderms (100 to 500 μm)	Low-Mg calcite	Non-luminescent	Pink stained, non-ferroan calcite	$FeCO_3$: 0 mol%; $MnCO_3$: 0·01 mol%, $MgCO_3$: 2·09 mol%; $SrCO_3$: 0·05 mol%	$\delta^{18}O$: −2·7‰ to −0·2‰ *median value: −0·8‰* $\delta^{13}C$: −3·1‰ to 2·3‰ *median value: 1‰*	Shallow marine Reduced conditions *Marine phreatic*
Ferroan dogtooth cements (FDC) to syntaxial cements	Dogtooth fringes (20 to 30 μm); syntaxial calcite overgrowth around echinoderms (100 to 500 μm)	Low-Mg calcite	Non-luminescent	Blue stained, ferroan calcite	$FeCO_3$: 0·38 mol%; $MnCO_3$: 0·02 mol%, $MgCO_3$: 2·04 mol%; $SrCO_3$: 0·03 mol%	$\delta^{18}O$: −2·4‰ to 0‰ *median value: −0·7‰* $\delta^{13}C$: −1·8‰ to 4·7‰ *median value: 1·6‰*	Shallow marine Reduced conditions *Marine phreatic*
Microsparitic ferroan geopetal cements (MFGC)	Asymmetrical microsparitic cements infilling space between grains – 200 μm to 1 mm	Low-Mg calcite	Dark brown luminescence	Blue stained, ferroan calcite	$FeCO_3$: 0·61 mol%; $MnCO_3$: 0·1 mol%, $MgCO_3$: 0·55 mol%; $SrCO_3$: 0·07 mol%	$\delta^{18}O$: −4·9‰ to −2·6‰ *median value: −4·3‰* $\delta^{13}C$: −6·8‰ to −2·7‰ *median value: −4·4‰*	Supratidal with soil horizon *Meteoric vadose*
Brown-luminescent banded dogtooth cements (BLBDC)	Dogtooth fringes (20 to 300 μm); syntaxial calcite overgrowth around echinoderms (100 μm to 1 mm)	Low-Mg calcite	Brown luminescence surrounded by a narrow (generally <10 μm) bright yellow band	Blue stained (ferroan calcite) to pink stained (non-ferroan calcite)	$FeCO_3$: 0·18 mol%; $MnCO_3$: 0·03 mol%, $MgCO_3$: 0·46 mol%; $SrCO_3$: 0·02 mol%	$\delta^{18}O$: −6·1‰ to −2·2‰ *median value: −4·5‰* $\delta^{13}C$: −12·7‰ to 6·4‰ *median value: 0·2‰*	Supratidal (non-permanent soil horizon) *Meteoric phreatic*

Table 1. (continued)

Cement/grain types	General characteristics	Original mineralogy	Cathodoluminescence	Alizarin/ferricyanide	Major elements (median value)	Carbon and oxygen stable isotopes	Environment of formation
Blocky calcite cements (BC)	Coarse crystalline – 100 μm to 3 mm	Low-Mg calcite	Orange luminescence to non-luminescent	Blue stained (ferroan calcite) to pink stained (non-ferroan calcite)	$FeCO_3$: 0·71 mol%; $MnCO_3$: 0·21 mol%, $MgCO_3$: 0·50 mol%; $SrCO_3$: 0·01 mol%	$\delta^{18}O$: −10·8‰ to −4·7‰ *median value: −5·6‰* $\delta^{13}C$: −6·5‰ to 1·6‰ *median value: 0·2‰*	*Burial*
Microsparitic non-ferroan geopetal cements (MNFGC)	Asymmetrical microsparitic cements infilling space between grains (200 μm to several millimetres) – also present as dogtooth crystals (10 to 200 μm)	Low-Mg calcite	Bright yellow luminescence	Pink stained, non-ferroan calcite	$FeCO_3$: 0·06 mol%; $MnCO_3$: 0·56 mol%, $MgCO_3$: 0·68 mol%; $SrCO_3$: 0 mol%	$\delta^{18}O$: −6·0‰ to −3·7‰ *median value: −4·9‰* $\delta^{13}C$: −13·6‰ to 0·9‰ *median value: −7·8‰*	*Exhumation*

ferroan syntaxial cements pre-dates the isopachous fibrous cements.

Discontinuity Bt2 (Middle Bathonian) is recorded at both Sites 2 and 3. At Site 2, discontinuity Bt2 is a planar surface with pendant cements. At Site 3, it is an erosional surface, under which abundant micritic envelopes formed along with micritic meniscus cements (*sensu* Hillgärtner *et al.*, 2001; Fig. 4C and D), pre-dating the dissolution of aragonitic shells. Micritic envelopes and meniscus-like cements are also associated with geopetal peloidal fabrics in small cavities. Non-ferroan dogtooth cements precipitated after the dissolution of aragonitic shells and are well-developed in dissolved shells but poorly so around grains. The subsequent phases are ferroan geopetal microsparitic cements and brown-luminescent banded dogtooth cements. In thin section, the erosional surface cross-cuts micritic envelopes, non-ferroan dogtooth cements and ferroan geopetal microsparitic cements. Microbial encrusting develops above this surface. Note that brown-luminescent banded cements occur both below and above this surface (Fig. 4C and D).

Discontinuity Bt3 (Late Bathonian) is recorded at both Sites 2 and 3. At Site 2, Bt3 is an erosive marine bored surface (Rioult *et al.*, 1991). At Site 3, Bt3 corresponds to a marine and erosive hardground (Fig. 4E and F). The underlying sediments display an intense micritization that precedes the development of isopachous fibrous cements around grains and then the dissolution of aragonite shells.

Discontinuity Bt4 (Late Bathonian) is recorded at Site 2, where it corresponds to a marine hardground (Andrieu *et al.*, 2016; Fig. 5A), and at Site 3 on core EST433, where it corresponds to an exposure surface. At Site 2, micritic envelopes formed along with meniscus-like cements below discontinuity Bt4, pre-dating the development of isopachous fibrous cements and then the dissolution of aragonitic shells. Non-ferroan dogtooth cements precipitated after the dissolution of aragonitic shells. At Site 3, discontinuity Bt4 corresponds to an erosion surface overlain by a lignite level (Fig. 5B). Non-luminescent sparitic meniscus cements developed along with non-isopachous dogtooth cements below this surface (Fig. 3).

Discontinuity Ox1 (Early Oxfordian) at Site 1 displays ferroan dogtooth cements that developed together with microsparitic bridge cements; they are followed by brown-luminescent banded dogtooth cements. Non-ferroan microsparitic geopetal cements post-date the formation of blocky calcite (Fig. 3).

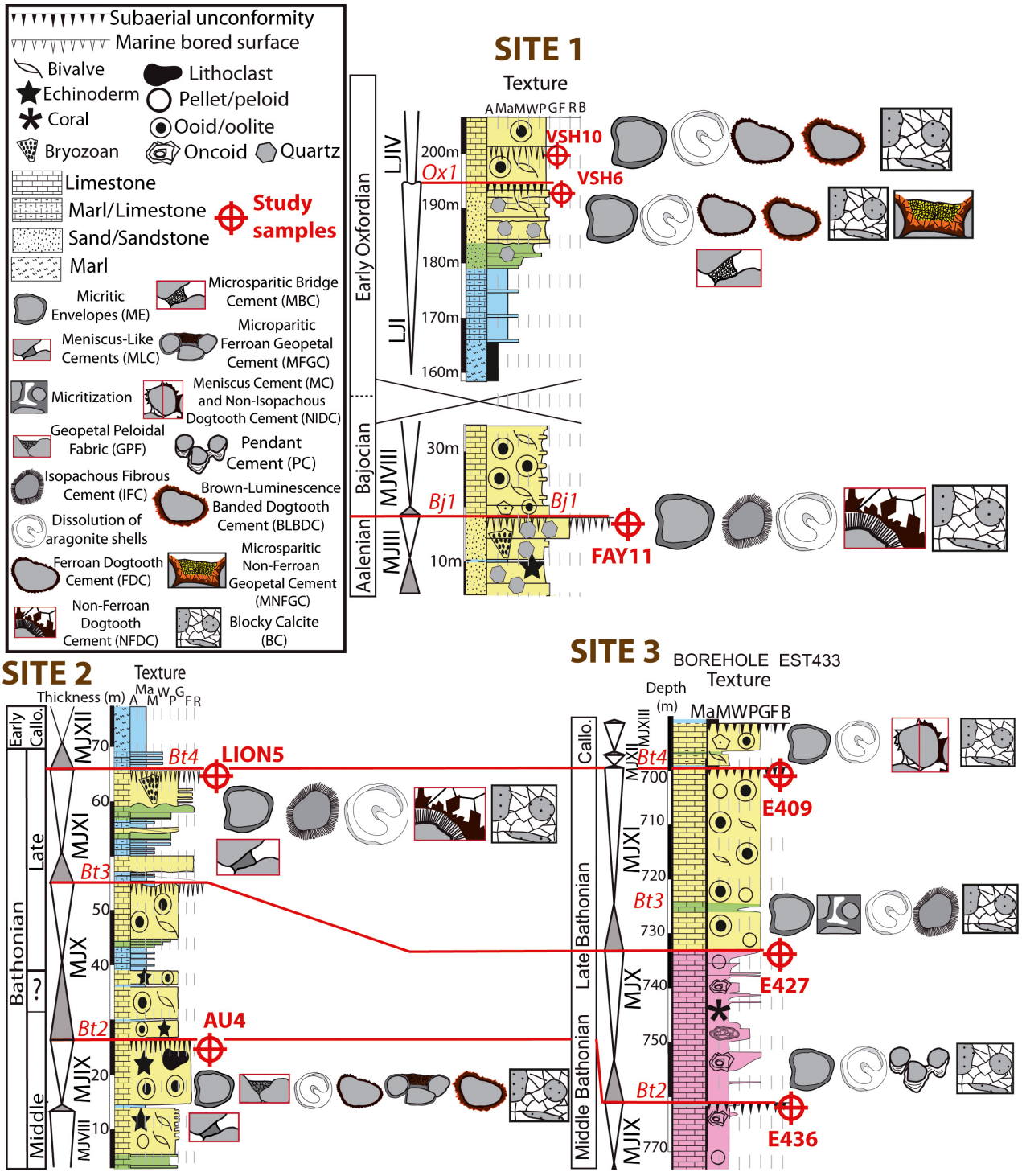

Fig. 3. Paragenetic sequences of the six thin sections under study located on the stratigraphic logs of the study areas. The log of Site 3 is modified from Brigaud *et al.* (2009a).

The sample VSH10 is from below a planar discontinuity that is not associated with a sequence boundary. Two generations of cements post-date the development of rare micritic envelopes and the dissolution of aragonitic shells: non-luminescent ferroan dogtooth cements and brown-luminescent banded dogtooth cements (Fig. 3).

Petrographic description, carbon and oxygen isotopes, and major element compositions of the diagenetic stages

All of the cements studied contain <4% $MgCO_3$ (Table 2). Cements are considered here as ferroan when they have a median $FeCO_3$ molar percentage higher than 0·3%. A total of 138 $\delta^{13}C$ and 148 $\delta^{18}O$ values are available for the 12 early cements and fabrics identified, as well as the blocky calcite (Table 3; Figs 6, 7 and 8).

Micritic envelopes (ME)

Micrite envelopes (50 to 100 μm thick; Fig. 9A and B) developed mostly around bivalve shells, peloids, lithoclasts and ooids. These fabrics are non-ferroan, with a pink colour after alizarin–potassium ferricyanide staining. The luminescence colour is orange (Fig. 9A and B). They are cross-cut by the hardground surface Bt2 (Site 2; Fig. 4C and D), thus indicating that they precipitated prior to erosion. Two $\delta^{13}C$ and $\delta^{18}O$ measurements were made on micritic envelopes. The $\delta^{18}O$ values are −1·4‰ and −1‰ (median: −1·2‰), and the $\delta^{13}C$ values are −20‰ and −3·4‰ (median: −11·7‰; Figs 6, 7, 8 and 10A). The molar percentages vary from 0·36 to 1·63% for $MgCO_3$ (median: 0·88%), 0·1 to 0·22% for $FeCO_3$ (median: 0·11%), 0 to 0·02% for $MnCO_3$ (median: 0·01%) and 0·02 to 0·04% for $SrCO_3$ (median: 0·04%; n = 3; Fig. 11).

Meniscus-like cements (MLC)

Meniscus-like cements (to distinguish them from sparitic vadose meniscus cements; *sensu* Hillgärtner *et al.*, 2001) form a micritic bridge between grains approximately 200 to 500 μm thick, sometimes displaying micropeloidal texture (Fig. 9A and B). These cements are non-ferroan and display an orange luminescence under cathodoluminescence (Fig. 9A). Their $\delta^{18}O$ values vary from −2·5‰ and −1·1‰ (median: −1·8‰; n = 5), and their $\delta^{13}C$ values are −17·8‰ and −0·1‰ (median: −12‰; n = 5; Figs 6, 7, 8 and 10A). The molar percentages are 0·15% for $FeCO_3$, 0·01% and 0·02% for $MnCO_3$, 1·27% and 1·29% for $MgCO_3$ and finally 0·03% and 0·04% for $SrCO_3$ (n = 2; Fig. 11).

Micritization

A stage of micritization filling a large part of intergranular space post-dates the development of micritic envelopes (Fig. 4E and F; sample FAY11). A hardground surface is cross-cutting the micritization stage (Fig. 4E and F) which is slightly more luminescent than the micritic envelopes, thus indicating that it precipitated prior to erosion.

Geopetal peloidal fabrics (GPF)

Meniscus-like cements and micritic envelopes are sometimes associated with peloidal to micropeloidal wackestones to packstones forming geopetal structures (200 to 500 μm thick; Fig. 9A and B); they are non-ferroan with an orange luminescence (Fig. 9A and B). The $\delta^{18}O$ value of these fabrics is −2·4‰, and the $\delta^{13}C$ is −15‰ (n = 1; Figs 6, 7 and 8). The molar percentages are 0·14% and 0·29% for $FeCO_3$, 0·01% and 0·02% for $MnCO_3$, 1·13% and 1·41% for $MgCO_3$, and finally 0·03% and 0·06% for $SrCO_3$ (n = 2; Fig. 11).

Isopachous fibrous cements (IFC)

These cements consist of thin isopachous fibrous fringes (50 to 100 μm thick) and are composed of inclusion-rich crystals associated with iron oxyhydroxides (Fig. 9C and D); they can also develop as syntaxial cements around echinoderms (50 to 200 μm thick). Isopachous fibrous cements exhibit cloudy brown to orange luminescence (Fig. 9C); they are ferroan, appearing blue with alizarin–potassium ferricyanide staining (Fig. 9D). The $\delta^{18}O$ values vary from −6‰ to +6‰ (median: −4·5‰; n = 13), and the $\delta^{13}C$ vary from −6·1‰ to +1·3‰ (median: −1·3‰; n = 12; Figs 6, 7, 8 and 12A). The molar percentages are from 0·48 to 0·67% for $FeCO_3$ (median: 0·55%), 0·20 to 0·37% for $MnCO_3$ (median: 0·25%), 0·43 to 0·57% for $MgCO_3$ (median: 0·56%) and 0·01 to 0·02% for $SrCO_3$ (median: 0·02; n = 2; Fig. 11).

Dissolution of aragonite shells

Mouldic dissolution of the aragonitic skeletal debris (mostly gastropods and bivalves) occurs in all of the studied limestones. The mouldic voids were successively filled with non-ferroan and ferroan dogtooth cements (Fig. 4C), brown-luminescent banded dogtooth cements and blocky cements, suggesting a very early process.

Pendant cements (PC)

Pendant cements form asymmetrical crusts several millimetres thick that are present within the coarse-grained oncoid and gastropod grainstone to rudstone of the Calcaires de Chaumont Formation (Site 3, E436; Fig. 13A). The cements are dominantly limpid and appear dark blue under CL and pink with alizarin–potassium

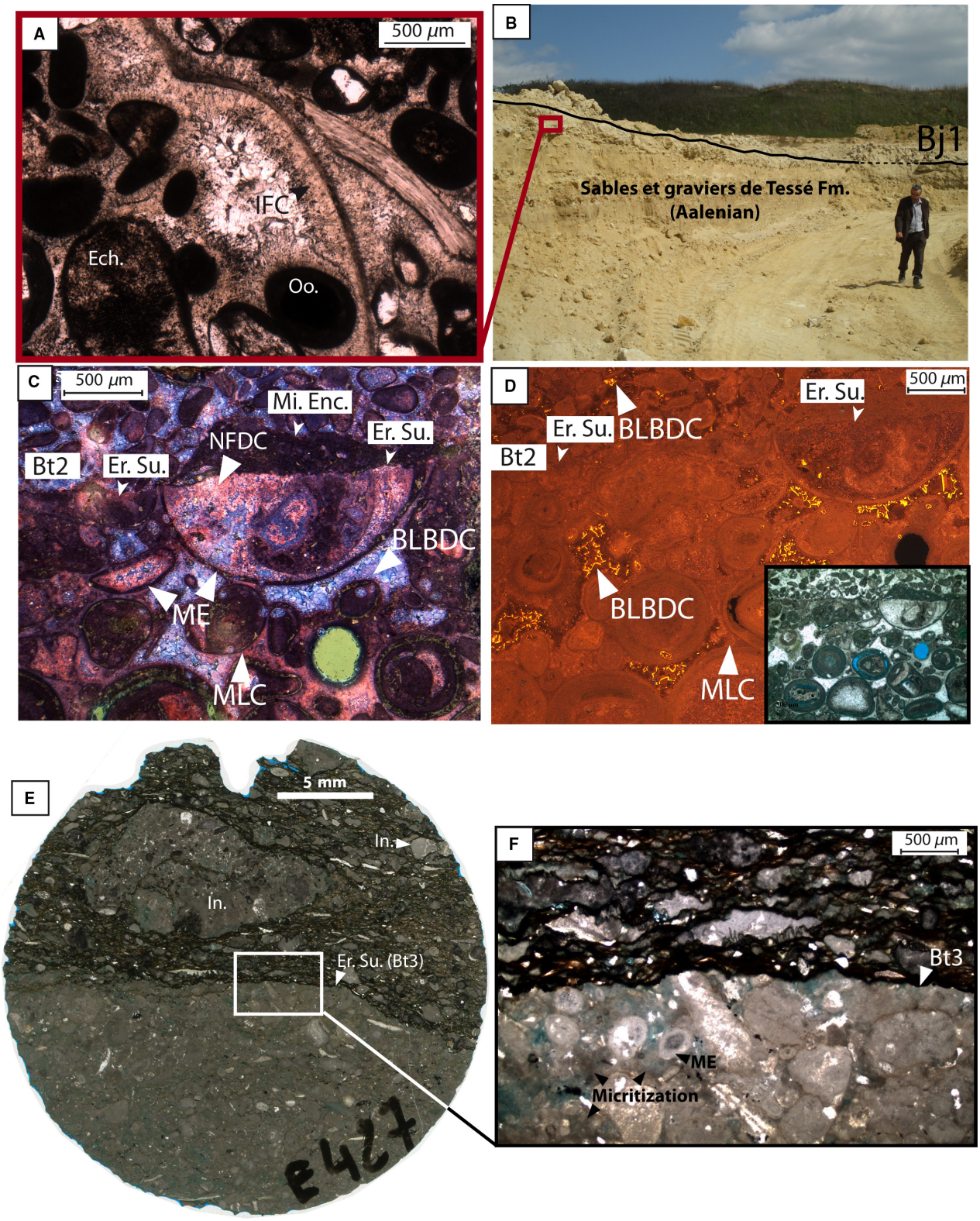

ferricyanide staining, and contain scattered narrow bands of fibrous crystals that appear light pink under CL. Micrometric growth lines are observed (Fig. 13A). The $\delta^{18}O$ values of pendant cements fluctuate between −6·6‰ and −1·9‰ (median: −4·1‰; Figs 6, 7 and 10B), whereas their $\delta^{13}C$ values fluctuate between −1·1‰ and +4·9‰ (median: +0·8‰; n = 12; Figs 5, 8

Fig. 4. (A) Oobioclastic grainstone with echinoderms (Ech.), ooids (Oo.) and isopachous fibrous cements (IFC), located below a perforated marine hardground; thin-section FAY11, Site 1, sequence boundary Bj1. (B) Marine hardground marking the sequence boundary Bj1 at the top of the Sables et Graviers de Tessé Formation – Site 1. Thin-section Au4, Site 2, sequence boundary Bt2, Calcaire de Blainville Formation, Bathonian. Person for scale is *ca* 1·8 m tall. (C) Alizarin–potassium ferricyanide stained view of an oobioclastic grainstone presenting MLC, BLBDC and an erosion surface (Er. Su.) cross-cutting NFDC and ME, with overlying by microbial encrustments (Mi. Enc.). (D) CL image of an oobioclastic grainstone presenting an erosion surface (Er. Su.), brown-luminescent dogtooth cements and meniscus-like cements. Thin-section E436, Site 3, Calcaire de Chaumont Formation, Bathonian. (E) Scan showing where the discontinuity Bt3 can be observed. The underlying sediments display an intense micritization, and intraclasts (In.) are present above the discontinuity. (F) Erosive surface Bt3 cross-cutting ME and micritization stages. MLC, meniscus-like cements; BLBDC, brown-luminescent banded dogtooth cements; NFDC, non-ferroan dogtooth cements, ME, micritic envelopes.

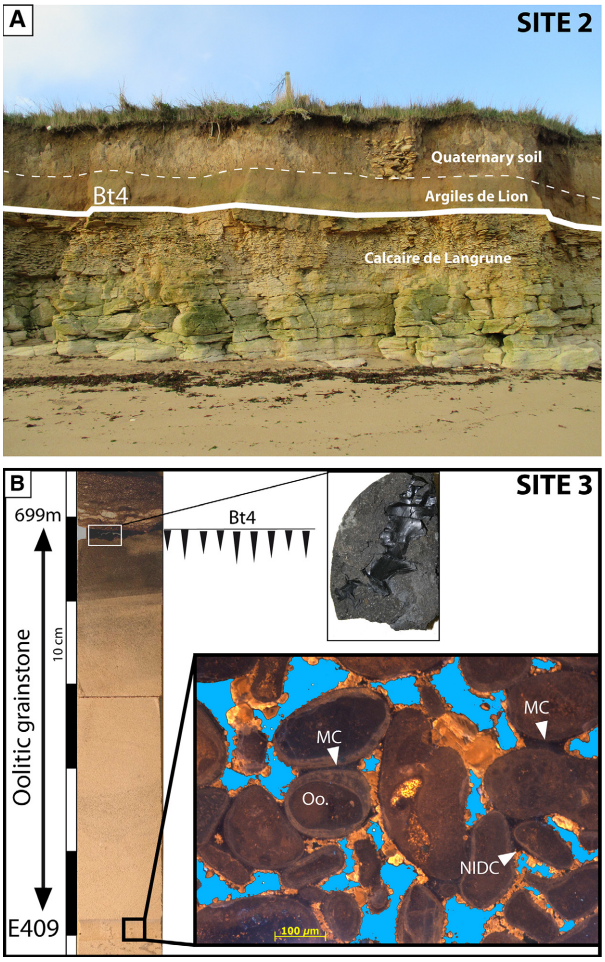

Fig. 5. (A) Marine discontinuity between the Calcaire de Langrune and the Argiles de Lion Formation marking the sequence boundary Bt4 – Site 2. (B) Drill core with the location of: (i) the erosional discontinuity Bt4 topped by a lignite level; and (ii) sample E409, displaying meniscus cements (MC), non-isopachous dogtooth cements (NIDC) and ooids (Oo.).

and 10B). The molar percentages are between 0% and 0·26% for $FeCO_3$ (median: 0%), 1·30% and 3·63% for $MgCO_3$ (median: 2·07%) and between 0·03% and 0·12% for $SrCO_3$ (median: 0·06%; n = 11; Fig. 11). The molar percentage of $MnCO_3$ is zero.

Microsparitic bridge cements (MBC)

These are non-isopachous microsparitic cements forming bridges between ooids (100 μm to 1 mm; Fig. 13B and C). Cements are clear, non-luminescent (Fig. 13B) and slightly ferroan (slightly blue when stained with alizarin–potassium ferricyanide; Fig. 13C). Their shapes do not correspond to concave menisci typical of vadose settings (Purser, 1969), but to more elongated bridges similar to meniscus-like cements described by Hillgärtner *et al.* (2001). Microsparitic bridge cements display $\delta^{18}O$ values ranging from 0 to −4·1‰ (median: −1·7‰; n = 11) and $\delta^{13}C$ values ranging from −0·9‰ to +4·2‰ (median: +1·7‰; n = 8; Figs 5, 6, 7 and 12B). The molar percentages of $MnCO_3$ and $SrCO_3$ are 0·02% (n = 2), whereas the molar percentages of $FeCO_3$ are 0·12% and 0·3%, and the molar percentages of $MgCO_3$ are 0·5% and 2·0% (n = 2; Fig. 11).

Meniscus cements (MC)

Sparitic meniscus cements, hundreds of microns in size, are present at Site 3 (E409; Fig. 13D). These cements are non-luminescent, non-ferroan and limpid (Fig. 13D). The oxygen isotope composition values range from −5·5 to −3·6‰ (median: −4·3‰; n = 9; Fig. 6) and $\delta^{13}C$ values from −14·8 to −4·4‰ (median: −5·5‰; n = 9; Figs 5, 7 and 14). The molar percentage ranges from 0·02 to 0·13% for $FeCO_3$ (median: 0·02%), 0 to 0·2% for $MnCO_3$ (median: 0%), 0·60 to 0·96% for $MgCO_3$ (median: 0·81%) and 0·01 to 0·03% for $SrCO_3$ (median: 0·02; n = 5; Fig. 11).

Non-isopachous dogtooth cements (NIDC)

At Site 3 (E409, Figs 13D and 14), meniscus cements are associated with non-isopachous

Table 2. Molar percentages of $MgCO_3$, $MnCO_3$, $FeCO_3$, $SrCO_3$ and $CaCO_3$ in the different cement stages and samples.

Cement stage	Sample	$FeCO_3$ (%)	$MnCO_3$ (%)	$MgCO_3$ (%)	$SrCO_3$ (%)	$CaCO_3$ (%)
Micritic Envelope (ME)	E409	0·11	0·00	0·36	0·02	80·7
Micritic Envelope (ME)	AU4	0·10	0·01	1·63	0·04	94·5
Micritic Envelope (ME)	AU4	0·22	0·02	0·88	0·04	83·0
Meniscus-Like Cement (MLC)	AU4	0·15	0·01	1·29	0·04	95·6
Meniscus-Like Cement (MLC)	AU4	0·15	0·02	1·27	0·03	94·2
Geopetal Peloidal Fabric (GPF)	AU4	0·14	0·02	1·41	0·06	95·9
Geopetal Peloidal Fabric (GPF)	AU4	0·29	0·01	1·13	0·03	89·8
Isopachous Fibrous Cement (IFC)	FAY-11	0·67	0·37	0·43	0·02	93·6
Isopachous Fibrous Cement (IFC)	FAY-11	0·48	0·20	0·56	0·01	94·1
Isopachous Fibrous Cement (IFC)	FAY-11	0·55	0·25	0·57	0·02	93·6
Pendant Cement (PC) – blue luminescence	E436	0·00	0·00	1·28	0·03	96·4
Pendant Cement (PC) – blue luminescence	E436	0·26	0·00	1·39	0·12	95·9
Pendant Cement (PC) – blue luminescence	E436	0·00	0·00	2·23	0·06	94·8
Pendant Cement (PC) – blue luminescence	E436	0·00	0·00	2·09	0·07	95·4
Pendant Cement (PC) – blue luminescence	E436	0·00	0·00	2·74	0·09	94·4
Pendant Cement (PC) – blue luminescence	E436	0·00	0·00	3·63	0·08	94·1
Pendant Cement (PC) – blue luminescence	E436	0·01	0·00	3·05	0·08	94·2
Pendant Cement (PC) – pink luminescence	E436	0·02	0·00	1·43	0·03	95·8
Pendant Cement (PC) – pink luminescence	E436	0·00	0·01	2·07	0·05	95·2
Pendant Cement (PC) – pink luminescence	E436	0·00	0·00	1·43	0·05	95·8
Pendant Cement (PC) – pink luminescence	E436	0·17	0·00	1·30	0·03	94·1
Microsparitic Bridge Cement (MBC)	VSH6	0·30	0·02	2·00	0·02	94·8
Microsparitic Bridge Cement (MBC)	VSH6	0·12	0·02	0·50	0·02	95·5
Meniscus Cement (MC)	E409	0·02	0·00	0·60	0·03	97·3
Meniscus Cement (MC)	E409	0·02	0·00	0·81	0·02	97·1
Meniscus Cement (MC)	E409	0·03	0·00	0·73	0·01	96·6
Meniscus Cement (MC)	E409	0·13	0·02	0·92	0·02	95·0
Meniscus Cement (MC)	E409	0·01	0·00	0·96	0·02	96·9
Non-Ferroan Dogtooth Cement (NFDC)	FAY-11	0·00	0·01	1·62	0·05	95·1
Non-Ferroan Dogtooth Cement (NFDC)	FAY-11	0·00	0·02	2·52	0·05	95·1
Non-Ferroan Dogtooth Cement (NFDC)	FAY-11	0·00	0·00	2·49	0·10	94·3
Non-Ferroan Dogtooth Cement (NFDC)	FAY-11	0·01	0·03	0·89	0·04	94·9
Non-Ferroan Dogtooth Cement (NFDC)	FAY-11	0·01	0·01	2·09	0·04	95·4
Ferroan Dogtooth Cement (FDC)	VSH6	0·24	0·02	2·14	0·03	95·6
Ferroan Dogtooth Cement (FDC)	VSH6	0·13	0·00	1·55	0·04	89·3
Ferroan Dogtooth Cement (FDC)	VSH6	0·30	0·02	1·59	0·05	95·6
Ferroan Dogtooth Cement (FDC)	VSH10	0·77	0·05	2·22	0·03	92·8
Ferroan Dogtooth Cement (FDC)	VSH10	0·61	0·03	2·14	0·03	93·5
Ferroan Dogtooth Cement (FDC)	VSH10	0·47	0·02	1·93	0·02	92·9
Microsparitic Ferroan Geopetal Cement (MFGC)	AU4	0·61	0·01	0·63	0·07	93·8
Microsparitic Ferroan Geopetal Cement (MFGC)	AU4	0·65	0·01	0·52	0·07	93·0
Microsparitic Ferroan Geopetal Cement (MFGC)	AU4	0·59	0·01	0·55	0·05	93·3
Brown-Luminescence Banded Dogtooth Cement (BLBDC)	AU4	0·36	0·01	0·21	0·02	94·8
Brown-Luminescence Banded Dogtooth Cement (BLBDC)	AU5	0·37	0·02	0·17	0·01	95·1
Brown-Luminescence Banded Dogtooth Cement (BLBDC)	AU6	0·75	0·30	0·11	0·01	93·6
Brown-Luminescence Banded Dogtooth Cement (BLBDC)	VSH6	0·16	0·03	0·91	0·02	96·7
Brown-Luminescence Banded Dogtooth Cement (BLBDC)	VSH7	0·18	0·03	1·02	0·01	95·9
Brown-Luminescence Banded Dogtooth Cement (BLBDC)	VSH8	0·02	0·02	0·46	0·02	97·4
Brown-Luminescence Banded Dogtooth Cement (BLBDC)	VSH9	0·18	0·03	1·01	0·02	94·9
Blocky Calcite (BC)	E409	0·0	0·00	0·75	0·11	97·3
Blocky Calcite (BC)	AU4	1·35	0·03	0·25	0·03	92·6
Blocky Calcite (BC)	AU4	0·73	0·04	0·04	0·00	95·2
Blocky Calcite (BC)	FAY11	0·71	1·87	0·51	0·01	90·6
Blocky Calcite (BC)	FAY11	0·64	2·03	0·50	0·01	91·2
Blocky Calcite (BC)	FAY11	0·93	0·42	0·99	0·01	92·0
Blocky Calcite (BC)	FAY11	0·35	0·21	0·21	0·00	95·0
Microsparitic Non-Ferroan geopetal Cement (MNFGC)	VSH6	0·05	0·80	0·68	0·00	93·2
Microsparitic Non-Ferroan geopetal Cement (MNFGC)	VSH6	0·07	1·04	0·67	0·00	92·8

dogtooth cements (10 to 20 μm long), which are not present all around the grains. These cements are non-luminescent, non-ferroan and limpid (Figs 13D and 14).

Non-ferroan dogtooth cements (NFDC) and ferroan dogtooth cements (FDC)

These cements are limpid crystals forming isopachous fringes around grains (Fig. 9C and D; 15A to D). The hardground surface Bt2 (Site 2, Fig. 4C and D) is cross-cutting non-ferroan dogtooth cements, thus indicating that these precipitated before the abrasion process. Ferroan dogtooth cements are 20 to 30 μm long and non-luminescent (Fig. 15A to D), whereas non-ferroan dogtooth cements are 20 to 200 μm long and non-luminescent (Fig. 9C and D). Around echinoderms, 50 μm to 1 mm long syntaxial overgrowth cements developed contemporaneously to the dogtooth fringes (Figs 9D and 12A to C). An early generation of non-ferroan and non-luminescent syntaxial cement pre-dates the fibrous cements, but is only found in thin-section FAY11 (Fig. 9D). Oxygen isotope composition values range from −2·7 to −0·2‰ (median: −0·8‰; n = 9; Figs 6, 7 and 12A to C) for non-ferroan dogtooth cements and from −2·4 to 0‰ (median: −0·7‰; n = 23; Figs 6, 7 and 12A to C) for ferroan dogtooth cements. Carbon isotope composition values range from −3·1‰ to +2·3‰ (median: +1‰; n = 9) for non-ferroan dogtooth cements and from −1·8‰ to +4·7‰ (median: +1·6‰; n = 21) for ferroan dogtooth cements (Figs 6, 8 and 12A to C). For non-ferroan dogtooth cements, the molar percentages range from 0 to 0·1% for $FeCO_3$ (median: 0%), 0 to 0·03% for $MnCO_3$ (median: 0·01%), 0·89 to 2·52% for $MgCO_3$ (median: 2·09%) and 0·04 to 1·0% for $SrCO_3$ (median: 0·05%; n = 5; Fig. 11). In ferroan dogtooth cements, the molar percentage varies from 0·13 to 0·77% for $FeCO_3$ (median: 0·38%), 0 to 0·05% for $MnCO_3$ (median: 0·02%), 1·55 to 2·22% for $MgCO_3$ (median: 2·04%) and 0·02 to 0·05% for $SrCO_3$ (median: 0·03; n = 6; Fig. 11).

Microsparitic ferroan geopetal cements (MFGC)

Microsparitic ferroan geopetal cements are limpid, microsparitic and range in size from hundreds of microns to several millimetres (Figs 9A, 9B and 10A). These cements display brown luminescence and are located in small cavities between grains (Figs 9A, 9B and 10A) in contrast to pendant cements. They are cross-cut by the hardground surface Bt2 (Site 2, Fig. 4C and D), thus indicating that they precipitated before erosion. The $\delta^{18}O$ values range from −6·0 to −3·7‰ (median: −4·3‰; n = 13) and the $\delta^{13}C$ values from −13·6‰ to +0·9‰ (median: −4·4‰; n = 13; Figs 6, 7, 8 and 10A). The molar percentages vary from 0·59 to 0·65% for $FeCO_3$ (median: 0·61%). They are 0·1% for MnCO3, and they vary from 0·52 to 0·63% for $MgCO_3$ (median: 0·55%) and from 0·05 to 0·07% for $SrCO_3$ (median: 0·07%; n = 3; Fig. 11).

Brown-luminescent banded dogtooth cements (BLBDC)

Brown-luminescent banded dogtooth cements are 20 to 300 μm long and display a mostly brown luminescence surrounded by a narrow band with bright yellow to orange luminescence (*ca* 10 μm, Figs 9A, 10A, 12B to C, 15C and 16A). The crystals display varying alizarin–potassium ferricyanide staining from blue to violet or pink, which reflects variations in iron content (Figs 9B, 15B and 16B). These cements, forming isopachous fringes around grains, developed contemporaneously as 50 μm to 1 mm long syntaxial overgrowth cements around echinoderms (Figs. 12B, 12C, 16A and 16B). The $\delta^{18}O$ values fluctuate from −6·1 to −2·2‰ (median: −4·5‰; n = 32), while the $\delta^{13}C$ values range from −12·7‰ to +6·4‰ (median: +0·2‰; n = 31; Figs 6, 7, 8, 10A, 12A and 12B). The molar percentages range from 0·02 to 0·75% for $FeCO_3$ (median: 0·18%), 0·01 to 0·3% for $MnCO_3$ (median: 0·03%), 0·11 to 1·02% for $MgCO_3$ (median: 0·46%) and 0·1 to 0·02% for $SrCO_3$ (median: 0·02%; n = 2; Fig. 11).

Blocky calcite cements (BC)

Blocky calcite cements occur within the intergranular and intragranular pores in all of the thin sections. This cement phase is formed by coarse ferroan to non-ferroan crystals (100 μm to several millimetres in thickness; Figs 9B to C, 10A, 10B and 15A). Luminescence patterns reveal several growth stages during their precipitation: orange, brown and dark brown, marking varying amounts of iron incorporation within the calcite lattice during burial (Figs 9, 10A, 10B, 12, 14 and 15B). Syntaxial overgrowth developed around echinoderms contemporaneously with blocky calcite, after early syntaxial subzones. The $\delta^{18}O$ values range between −10·8‰ and −4·7‰ (median: −5·6‰; n = 13), while the $\delta^{13}C$ values fluctuate between −6·5‰ and +1·6‰ (median: +0·2‰; n = 10; Figs 6, 7, 8, 10A, 10B, 12A, 12B and 14). The molar percentages range from 0 to 1·35% for

Table 3. Sample and cement stage location of the analysis, and associated $\delta^{18}O$ and $\delta^{13}C$ values.

Cement stage	Sample	$\delta^{18}O$ (‰ versus PDB)	$\delta^{13}C$ (‰ versus PDB)
Micritic Envelope (ME)	AU4	−1·4	−20·0
Micritic Envelope (ME)	AU4	−1·0	−3·4
Meniscus-Like Cement (MLC)	AU4	−2·5	−17·8
Meniscus-Like Cement (MLC)	AU4	−2·1	−6·7
Meniscus-Like Cement (MLC)	AU4	−1·8	−14·4
Meniscus-Like Cement (MLC)	AU4	−1·1	−12·0
Meniscus-Like Cement (MLC)	AU4	−1·2	−0·1
Geopetal Peloidal Fabric (GPF)	AU4	−2·4	−15·0
Isopachous Fibrous Cement (IFC)	FAY11	−3·0	−0·1
Isopachous Fibrous Cement (IFC)	FAY11	−5·3	1·3
Isopachous Fibrous Cement (IFC)	FAY11	−3·0	−2·7
Isopachous Fibrous Cement (IFC)	FAY11	−3·1	−0·4
Isopachous Fibrous Cement (IFC)	FAY11	−6·0	−3·8
Isopachous Fibrous Cement (IFC)	FAY11	−5·9	0·2
Isopachous Fibrous Cement (IFC)	FAY11	−4·0	0·5
Isopachous Fibrous Cement (IFC)	FAY11	−4·2	−3·0
Isopachous Fibrous Cement (IFC)	FAY11	−5·7	−5·9
Isopachous Fibrous Cement (IFC)	FAY11	−4·5	−6·1
Isopachous Fibrous Cement (IFC)	FAY11	−5·6	−5·4
Isopachous Fibrous Cement (IFC)	FAY11	−2·8	−1·3
Isopachous Fibrous Cement (IFC)	FAY11	−5·4	−0·3
Pendant Cement (PC) – violet luminescence	E436	−4·5	−1·0
Pendant Cement (PC) – violet luminescence	E436	−4·1	−0·2
Pendant Cement (PC) – violet luminescence	E436	−4·0	0·0
Pendant Cement (PC) – violet luminescence	E436	−4·7	1·9
Pendant Cement (PC) – violet luminescence	E436	−3·6	0·9
Pendant Cement (PC) – violet luminescence	E436	−5·4	3·0
Pendant Cement (PC) – violet luminescence	E436	−4·1	4·9
Pendant Cement (PC) – violet luminescence	E436	−3·5	−1·1
Pendant Cement (PC) – violet luminescence	E436	−6·6	0·7
Pendant Cement (PC) – violet luminescence	E436	−3·2	0·9
Pendant Cement (PC) – pink luminescence	E436	−1·9	1·4
Pendant Cement (PC) – pink luminescence	E436	−2·5	−0·3
Microparitic Bridge Cement (MBC)	VSH6	−0·5	2·8
Microparitic Bridge Cement (MBC)	VSH6	−1·3	−0·9
Microparitic Bridge Cement (MBC)	VSH6	−1·7	3·0
Microparitic Bridge Cement (MBC)	VSH6	0·0	0·6
Microparitic Bridge Cement (MBC)	VSH6	−2·9	4·2
Microparitic Bridge Cement (MBC)	VSH6	−0·4	−0·5
Microparitic Bridge Cement (MBC)	VSH6	−3·3	3·6
Microparitic Bridge Cement (MBC)	VSH6	−0·6	0·6
Microparitic Bridge Cement (MBC)	VSH6	−3·3	–
Microparitic Bridge Cement (MBC)	VSH6	−4·0	–
Microparitic Bridge Cement (MBC)	VSH6	−4·1	–
Meniscus Cement (MC)	E409	−3·8	−5·6
Meniscus Cement (MC)	E409	−4·3	−6·5
Meniscus Cement (MC)	E409	−3·7	−5·3
Meniscus Cement (MC)	E409	−3·6	−4·6
Meniscus Cement (MC)	E409	−4·4	–
Meniscus Cement (MC)	E409	−4·1	−8·5
Meniscus Cement (MC)	E409	−4·4	−4·4
Meniscus Cement (MC)	E409	−4·7	−14·8
Meniscus Cement (MC)	E409	−5·5	−5·2
Non-Ferroan Dogtooth Cement (NFDC)	FAY11	−0·4	1·3
Non-Ferroan Dogtooth Cement (NFDC)	FAY11	−0·8	−0·3
Non-Ferroan Dogtooth Cement (NFDC)	FAY11	−1·9	−1·1
Non-Ferroan Dogtooth Cement (NFDC)	FAY11	−0·8	1·2
Non-Ferroan Dogtooth Cement (NFDC)	FAY11	−0·2	1·0
Non-Ferroan Dogtooth Cement (NFDC)	FAY11	−0·5	−3·1
Non-Ferroan Dogtooth Cement (NFDC)	FAY11	−0·8	2·3
Non-Ferroan Dogtooth Cement (NFDC)	FAY11	−0·5	−1·4
Non-Ferroan Dogtooth Cement (NFDC)	FAY11	−2·7	1·0
Ferroan Dogtooth Cement (FDC)	VSH6	−0·2	2·0
Ferroan Dogtooth Cement (FDC)	VSH6	−0·7	1·3
Ferroan Dogtooth Cement (FDC)	VSH6	0·0	1·3
Ferroan Dogtooth Cement (FDC)	VSH6	−2·4	0·1
Ferroan Dogtooth Cement (FDC)	VSH6	−0·6	1·0
Ferroan Dogtooth Cement (FDC)	VSH6	−0·1	–
Ferroan Dogtooth Cement (FDC)	VSH6	−1·9	1·2
Ferroan Dogtooth Cement (FDC)	VSH6	−0·8	2·3
Ferroan Dogtooth Cement (FDC)	VSH6	−0·5	−1·8

Table 3. (continued)

Cement stage	Sample	$\delta^{18}O$ (‰ versus PDB)	$\delta^{13}C$ (‰ versus PDB)
Ferroan Dogtooth Cement (FDC)	VSH6	−0·3	1·6
Ferroan Dogtooth Cement (FDC)	VSH6	−1·5	0·9
Ferroan Dogtooth Cement (FDC)	VSH10	−1·1	2·4
Ferroan Dogtooth Cement (FDC)	VSH10	−0·3	1·1
Ferroan Dogtooth Cement (FDC)	VSH10	−0·6	2·5
Ferroan Dogtooth Cement (FDC)	VSH10	−0·7	3·9
Microparitic Ferroan Geopetal Cement (MFGC)	AU4	−4·7	−6·1
Microparitic Ferroan Geopetal Cement (MFGC)	AU4	−3·9	−6·8
Microparitic Ferroan Geopetal Cement (MFGC)	AU4	−5·7	−2·5
Microparitic Ferroan Geopetal Cement (MFGC)	AU4	−2·6	−4·5
Microparitic Ferroan Geopetal Cement (MFGC)	AU4	−2·7	−2·7
Microparitic Ferroan Geopetal Cement (MFGC)	AU4	−4·9	−4·2
Brown-Luminescence Banded Dogtooth Cement (BLBDC)	VSH6	−4·5	4·7
Brown-Luminescence Banded Dogtooth Cement (BLBDC)	VSH6	−4·5	3·9
Brown-Luminescence Banded Dogtooth Cement (BLBDC)	VSH6	−4·7	5·8
Brown-Luminescence Banded Dogtooth Cement (BLBDC)	VSH6	−4·0	−2·0
Brown-Luminescence Banded Dogtooth Cement (BLBDC)	VSH6	−4·4	−7·5
Brown-Luminescence Banded Dogtooth Cement (BLBDC)	VSH6	−4·0	4·0
Brown-Luminescence Banded Dogtooth Cement (BLBDC)	VSH6	−4·7	3·0
Brown-Luminescence Banded Dogtooth Cement (BLBDC)	VSH6	−4·4	−4·3
Brown-Luminescence Banded Dogtooth Cement (BLBDC)	VSH6	−2·2	−3·9
Brown-Luminescence Banded Dogtooth Cement (BLBDC)	VSH6	−4·7	−0·5
Brown-Luminescence Banded Dogtooth Cement (BLBDC)	VSH6	−4·5	−6·7
Brown-Luminescence Banded Dogtooth Cement (BLBDC)	VSH6	−4·9	3·8
Brown-Luminescence Banded Dogtooth Cement (BLBDC)	VSH6	−4·3	1·5
Brown-Luminescence Banded Dogtooth Cement (BLBDC)	VSH6	−3·1	2·0
Brown-Luminescence Banded Dogtooth Cement (BLBDC)	VSH6	−3·0	6·4
Brown-Luminescence Banded Dogtooth Cement (BLBDC)	VSH6	−5·0	3·5
Brown-Luminescence Banded Dogtooth Cement (BLBDC)	VSH6	−5·0	5·9
Brown-Luminescence Banded Dogtooth Cement (BLBDC)	VSH6	−2·9	–
Brown-Luminescence Banded Dogtooth Cement (BLBDC)	VSH6	−4·4	2·5
Brown-Luminescence Banded Dogtooth Cement (BLBDC)	VSH6	−3·6	−12·7
Brown-Luminescence Banded Dogtooth Cement (BLBDC)	VSH6	−4·1	−8·8
Brown-Luminescence Banded Dogtooth Cement (BLBDC)	VSH6	−2·9	−2·3
Brown-Luminescence Banded Dogtooth Cement (BLBDC)	VSH6	−4·8	−0·4
Brown-Luminescence Banded Dogtooth Cement (BLBDC)	VSH6	−5·3	0·2
Brown-Luminescence Banded Dogtooth Cement (BLBDC)	VSH6	−4·7	−8·0
Brown-Luminescence Banded Dogtooth Cement (BLBDC)	VSH6	−5·4	−3·0
Brown-Luminescence Banded Dogtooth Cement (BLBDC)	VSH6	−4·8	0·0
Brown-Luminescence Banded Dogtooth Cement (BLBDC)	VSH6	−3·5	0·2
Brown-Luminescence Banded Dogtooth Cement (BLBDC)	VSH6	−4·4	5·9
Brown-Luminescence Banded Dogtooth Cement (BLBDC)	VSH6	−4·4	0·9
Brown-Luminescence Banded Dogtooth Cement (BLBDC)	VSH6	−5·8	2·6
Brown-Luminescence Banded Dogtooth Cement (BLBDC)	VSH6	−6·1	−0·9
Blocky Calcite (BC)	VSH6	−7·5	–
Blocky Calcite (BC)	VSH6	−9·6	–
Blocky Calcite (BC)	VSH6	−8·6	–
Blocky Calcite (BC)	AU4	−4·7	−1·0
Blocky Calcite (BC)	AU4	−7·3	−6·5
Blocky Calcite (BC)	AU4	−5·2	3·0
Blocky Calcite (BC)	E409	−10·8	−0·1
Blocky Calcite (BC)	FAY11	−5·5	1·6
Blocky Calcite (BC)	FAY11	−5·8	1·3
Blocky Calcite (BC)	FAY11	−4·9	1·0
Blocky Calcite (BC)	FAY11	−4·8	0·0
Blocky Calcite (BC)	FAY11	−4·7	0·3
Blocky Calcite (BC)	FAY11	−5·6	−2·0
Microsparitic Non-Ferroan Geopetal Cement (MNFGC)	VSH6	−4·8	−10·6
Microsparitic Non-Ferroan Geopetal Cement (MNFGC)	VSH6	−6·0	−7·6
Microsparitic Non-Ferroan Geopetal Cement (MNFGC)	VSH6	−5·0	−8·8
Microsparitic Non-Ferroan Geopetal Cement (MNFGC)	VSH6	−5·0	−12·6
Microsparitic Non-Ferroan Geopetal Cement (MNFGC)	VSH6	−4·9	−7·6
Microsparitic Non-Ferroan Geopetal Cement (MNFGC)	VSH6	−4·4	−7·8
Microsparitic Non-Ferroan Geopetal Cement (MNFGC)	VSH6	−4·7	−5·6
Microsparitic Non-Ferroan Geopetal Cement (MNFGC)	VSH6	−4·9	−7·0
Microsparitic Non-Ferroan Geopetal Cement (MNFGC)	VSH6	−5·7	−6·5
Microsparitic Non-Ferroan Geopetal Cement (MNFGC)	VSH6	−4·8	−18·0
Microsparitic Non-Ferroan Geopetal Cement (MNFGC)	VSH6	−3·8	−13·6
Microsparitic Non-Ferroan Geopetal Cement (MNFGC)	VSH6	−3·7	0·9

$FeCO_3$ (median: 0·71%), from 0 to 2·03% for $MnCO_3$ (median: 0·21%), from 0·04 to 0·99% for $MgCO_3$ (median: 0·50%) and from 0·01 to 0·02% for $SrCO_3$ (median: 0·01%; n = 7; Fig. 11).

Microsparitic non-ferroan geopetal cements

Microsparitic non-ferroan geopetal cements in intergranular pores display a bright yellow luminescence and are non-ferroan (Fig. 16A and B). They post-date the development of blocky calcite. The $\delta^{18}O$ values range from −6·0 to −3·7‰ (median: −4·9‰; n = 13), and the $\delta^{13}C$ values vary from −13·6‰ to +0·9‰ (median: −7·8‰; n = 13; Figs 6, 7 and 8). The two molar percentage values are 0·05% and 0·07% for $FeCO_3$, 0·8% and 1·04% for $MnCO_3$, and 0·67% and 0·68% for $MgCO_3$ and 0% for $SrCO_3$ (n = 2; Fig. 11).

DISCUSSION: NEW PALAEOENVIRONMENTAL AND MINERALOGICAL INSIGHTS FROM THE $\delta^{18}O$ AND $\delta^{13}C$ SIGNALS OF EARLY CEMENTS

Temperatures and $\delta^{18}O$ of marine, mixed and meteoric parent fluids

Because oxygen isotopes fractionate during precipitation, an equilibrium fractionation diagram relating $\delta^{18}O$ PDB of calcite cements to precipitation temperatures is used to reconstruct the possible $\delta^{18}O$ SMOW of parent fluids (Fig. 17; Zheng, 1999). A seawater isotopic composition of −1‰ or 0‰ SMOW (Lécuyer *et al.*, 2003 and Dera *et al.*, 2011) was chosen for temperature calculation from the Kim & O'Neil (1997) fractionation equation. Following these assumptions, the seawater palaeotemperatures inferred from Paris Basin bivalve shells during the Middle and Late Jurassic range from 20 to 30°C (Brigaud *et al.*, 2008, 2009a). It is reasonable to assume that pore fluid temperatures and $\delta^{18}O$ values during the formation of early diagenetic cements in marine waters were close to seawater temperatures (20 to 30°C) and $\delta^{18}O$ values (−1‰ or 0‰; Fig. 17).

Since the seawater temperature values of 20 to 30°C are assumed on average for the Middle and Late Jurassic (Lécuyer *et al.*, 2003), a temperature range of 20 to 30°C, consistent with the present-day groundwater temperature at tropical to subtropical latitudes (Bahamas; Beddows *et al.*, 2007; Schubert & Jahren, 2015), is suggested for groundwater within the phreatic zone on isolated islands. The temperature of meteoric water in the vadose zone is assumed to be at least as high as in the phreatic zone. Presently, for latitudes of approximately 30 to 35°, corresponding to the palaeolatitude of the study area during the Middle and Late Jurassic (Thierry & Barrier, 2000), the rainfall $\delta^{18}O$ SMOW ranges from −6 to −3‰ SMOW (Gat *et al.*, 1994; Ayalon *et al.*, 1998; IAEA, 2000). Temperatures for mixed marine–meteoric groundwater may lie in the same range (20 to 30°C; Fig. 17) and could be characterized by an intermediate $\delta^{18}O$ value of −3·0 to −1·5‰ SMOW (Fig. 17).

Considering the equation of Zheng (1999), micritic fabrics (micritic envelopes, meniscus-like cements and geopetal peloidal fabrics), non-ferroan and ferroan dogtooth cements precipitated in marine to mixed water (Fig. 17A, E and F). Microsparitic bridge cements formed in marine to meteoric water (Fig. 17C). Pendant cements precipitated in meteoric to mixed water (Fig. 17B). Meniscus cements, microsparitic ferroan dogtooth cements and brown-luminescent banded dogtooth cements formed in meteoric water (Fig. 17F to H).

Initial mineralogy of micritic early cements in a calcite sea context

Micritic envelopes and meniscus-like cements (*sensu* Hillgärtner *et al.*, 2001) are the earliest cement phases as they pre-date the early dissolution of aragonite shells (Fig. 9A and B). These fabrics might have formed either in seawater or under very shallow burial conditions in a calcite sea (Sandberg, 1983; Palmer *et al.*, 1988; Dickson, 2004; Ferry *et al.*, 2007). Their stable oxygen isotope composition values (−2·5 to −1·0‰; median: −1·6‰) are in the range of non-recrystallized Jurassic bivalve $\delta^{18}O$ values recorded by numerous authors in western Tethyan basins (Dera *et al.*, 2011) and suggest a precipitation from Jurassic seawater (Fig. 17A). It is consistent with formation in a subtidal environment for meniscus-like cements and micritic envelopes, as suggested by Hillgärtner *et al.* (2001) when they are not associated with vadose cements (sparitic meniscus or pendant cements; Fig. 18). Carbon stable isotope values of early micritic fabrics display an exceptionally high variability from −20·0 to −0·1‰ (median: −13·2‰) but are always negative, indicating a relative enrichment in organic carbon of the calcite. Such a high variability of $\delta^{13}C$ cannot be evidenced using classical sampling methods such as microdrilling, but only by high-resolution ion

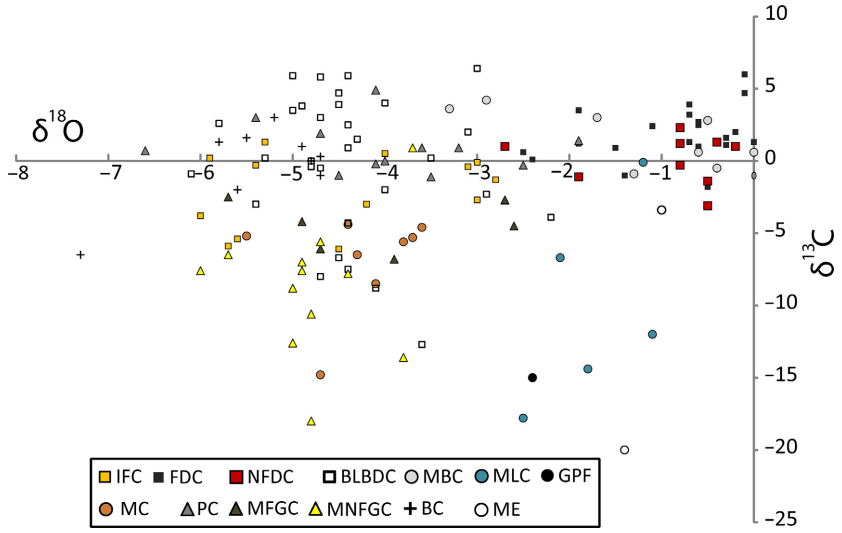

Fig. 6. $\delta^{18}O$ and $\delta^{13}C$ (‰-PDB) composition of the different cements and grain types: non-bioclastic grains, recrystallized bioclastic grains, micritic envelopes (ME), geopetal peloidal fabric (GPF), meniscus-like cements (MLC; *sensu* Hillgärtner *et al.*, 2001), isopachous fibrous cements (IFC), ferroan dogtooth to syntaxial cements (FDC), non-ferroan dogtooth to syntaxial cements (NFDC), microsparitic bridge cements (MBC), microsparitic ferroan geopetal cements (MFGC), meniscus cements (MC) and non-isopachous dogtooth cements (NIDC), pendant cement (PC), brown-luminescent banded dogtooth cements (BLBDC), microsparitic non-ferroan geopetal cements (MNFGC) and blocky calcite cementation (BC).

microprobe investigation. The resin (polyepoxide) present in the porosity could modify the $\delta^{13}C$ signature of the microporous micrite. The carbon isotope composition value of the polyepoxide cannot be measured using secondary ion mass spectrometry (SIMS) because the resin is almost instantly burned by the caesium ion beam. The molar percentage of $CaCO_3$ displays a high variability within micritic fabrics and cements, from 80·7 to 95·9% (Table 2), probably resulting from a variable rate of resin into the microporosity. Indeed, the micrite that appears bluish to green in transmitted light is characterized by the lowest $CaCO_3$ molar percentages (from 80·7 to 89·8%) and often by very negative $\delta^{13}C$ values (from −20·0 to −14·4‰). A doubt may be raised as to the meaning of these $\delta^{13}C$ values, which could result from the incorporation of the resin into the microporosity. However, some micritic fabrics and cement samples characterized by $CaCO_3$ molar percentages of about 95%, similar to those recorded in sparitic cements, also display negative $\delta^{13}C$ signatures (−12·0 to −0·1‰). Moreover, the $\delta^{18}O$ is relatively stable in all the micritic fabrics and cements investigated (−2·5 to −1·0‰). While the most negative $\delta^{13}C$ values of micritic cements and fabrics could partially result from the presence of resin in the microporosity, another factor must be proposed to explain the relative enrichment in organic carbon.

Micritic envelopes and meniscus-like cements are known as microbial induced fabric with a growth promoted by high organic-matter concentrations in the sediment (Hillgärtner *et al.*, 2001). Biogenically produced calcification is induced by modification of the environment around the microbes (Castanier, 1987; Ehrlich, 1996; Castanier *et al.*, 1997; Hillgärtner *et al.*, 2001). A wide range of bacterial processes, including ammonification, denitrification, sulphate reduction and anaerobic sulphide oxidation (Krumbein, 1979; Visscher *et al.*, 1992; Castanier *et al.*, 2000), can lead to HCO_3^- concentration and raised alkalinity, favouring $CaCO_3$ precipitation (von Knorre & Krumbein, 2000; Riding, 2000). These processes are localized within decaying mats as heterotrophic bacteria degrade organic matter (Bartley, 1996). The inorganic carbon (HCO_3^-) produced by these processes displays very low $\delta^{13}C$ values, since the source is organic matter (*ca* −25‰$_{PDB}$) and binds to carbonate cations to form carbonate minerals (Irwin *et al.*, 1977; Dupraz *et al.*, 2009). It explains the very negative $\delta^{13}C$ signal recorded in the resulting carbonate fabrics and cements, such as micritic envelopes or meniscus-like cements (Irwin *et al.*, 1977). The very high variability of $\delta^{13}C$ values in

micrite can be explained by: (i) a differential incorporation of organic carbon within calcite, potentially due to changes in bacterial processes (intensity, type); and (ii) the presence of resin (polyepoxide) in the microporosity that could tend to decrease the $\delta^{13}C$ signature.

Stable carbon and oxygen data were already acquired by microdrilling in microbially generated fabrics of the Triassic Latemar carbonate platform cycle tops (in northern Italy), showing very different signals in both $\delta^{18}O$, fluctuating between −5·1‰ and −2·9‰ (median: −3·7‰), and $\delta^{13}C$, ranging from +1·8 to +2·5‰ (median: +2·2‰) (Christ *et al.*, 2012a). The negative $\delta^{18}O$ values are explained by recrystallization of the former high-magnesium calcite mineralogy into low-magnesium calcite under the influence of meteoric fluids during diagenesis, as attested to by the patchy luminescence of microbial fabrics (Richter *et al.*, 2003; Christ *et al.*, 2012a). The $\delta^{13}C$ values of these cements do not, then, reflect their original signature. On the contrary, in the Paris Basin, the homogenous orange luminescence of microbially generated fabrics, as well as their high $\delta^{18}O$ signal and low $\delta^{13}C$ composition, indicates conservation of an initial low-magnesium mineralogy.

If these micritic cements had initially been in high-magnesium calcite or aragonite, they would have transformed into low-magnesium mineralogy in marine/meteoric water during early diagenesis or in basinal fluids during burial diagenesis, changing their $\delta^{18}O$ towards lower values (Tobin *et al.*, 1996; Loreau & Durlet, 1999). Their relatively high $\delta^{18}O$ (−2·5 to −1·0‰) indicates that no transformation occurred during burial or early exposure. Moreover, their $\delta^{13}C$ values would have been close to the marine carbon isotope ratio from 1 to 4‰ (Andrieu *et al.*, 2015; Navarro-Ramirez *et al.*, 2015) if stabilization had occurred in marine water, which is not the case as $\delta^{13}C$ values of micritic cements range from −20·0 to −0·1‰ (median: −13·2‰). The high $\delta^{18}O$ and very low $\delta^{13}C$ values of these micritic products argue for precipitation of low-magnesium calcite in marine water during deposition.

The transition from an aragonite sea to a calcite sea probably occurred during the early Jurassic (Sandberg, 1983; Wilkinson & Algeo, 1989; Dickson, 2002, 2004), and several studies already show that low-magnesium calcite could have precipitated directly in seawater during the Jurassic (Wilkinson *et al.*, 1985; Léonide *et al.*, 2012). It is thought that micrite crystals, which compose marine lime-mud, precipitated with an aragonitic or high-magnesium calcite mineralogy throughout the Phanerozoic (Folk, 1974; Bates & Brand, 1990). However, recent studies suggest that the shallow-marine micrite of lime-mud initially crystallized into low-magnesium calcite during the Cretaceous – as attested to by the similar morphology between lacustrine Miocene micrites and marine Cenomanian to early Turonian micrites (Volery *et al.*, 2009, 2010a,b, 2011) – and the Jurassic (Aalenian; Turpin *et al.*, 2014). Coimbra *et al.* (2009) show that Jurassic marine micrite can display high stable oxygen isotope ratios, but they interpret this as the consequence of early stabilization of micrite in low-magnesium calcite in seawater. The results of this study demonstrate that micritic products (micritic envelopes, geopetal peloidal fabric and meniscus-like cements) could directly precipitate into low-magnesium calcite in shallow-marine environments during the Middle Jurassic, and more specifically during the Bathonian.

Initial mineralogy of isopachous fibrous cement and timing of mineralogical transformation

Isopachous fibrous cements (IFC) are common in shallow carbonate platforms that developed during calcite sea periods (Sandberg, 1983; Dickson, 2004) and have been well-illustrated from the Middle Jurassic of the Paris Basin by Purser (1969) and Brigaud *et al.* (2009b). It is commonly thought that fibrous cements precipitate with an original aragonitic or high-magnesium calcite mineralogy from seawater (Folk, 1974; Durlet & Loreau, 1996). However, the new evidence of micritic envelopes and meniscus-like cements precipitating initially in low-magnesium calcite from seawater during the Jurassic questions this commonly held idea. Moreover, the timing of the mineralogical stabilization into low-magnesium calcite is discussed, as it may occur during burial or directly in seawater during calcite sea periods. The $\delta^{18}O$ values of isopachous fibrous cements (median: −4·5‰; n = 13), clearly lower than the values of the micritic fabrics (median: −1·6‰; n = 8), are similar to those measured in blocky calcite from the same sample (median $\delta^{18}O$ value: −5·2‰; n = 6). This feature, together with the absence of early emersion markers (sparitic meniscus cements, pendant cements, etc.), argues for recrystallization from an unstable precursor (aragonite or high-magnesium calcite) to a stable mineralogy (low-magnesium calcite) during burial. A seawater origin for their light $\delta^{18}O$

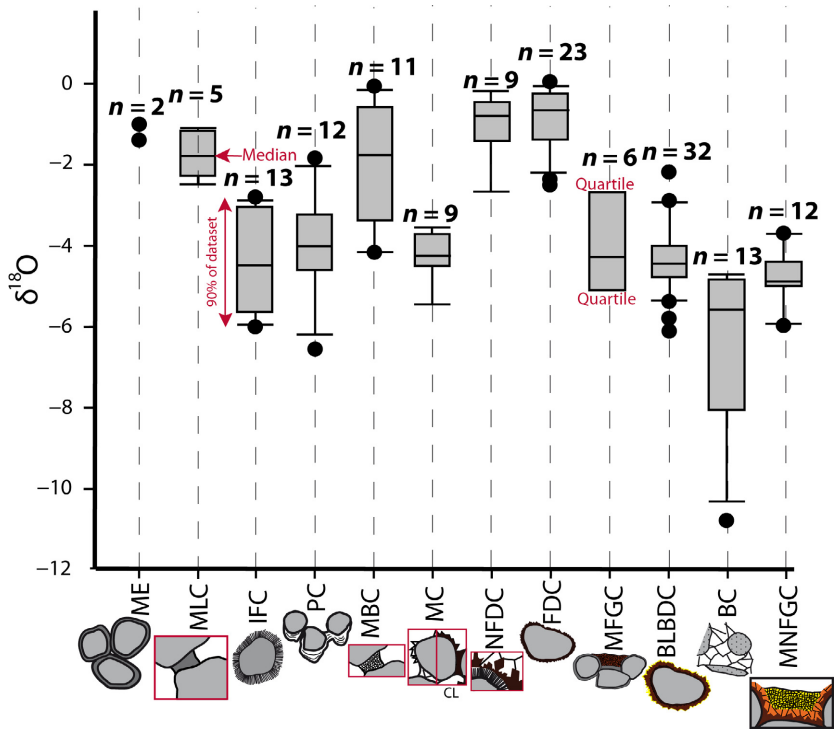

Fig. 7. $\delta^{18}O$ (‰-PDB) of the different cement types: micritic envelopes (ME), meniscus-like cements (MLC, *sensu* Hillgärtner *et al.*, 2001), isopachous fibrous cements (IFC), pendant cement (PC), microsparitic bridge cements (MBC), meniscus cements (MC), non-ferroan dogtooth to syntaxial cements (NFDC), ferroan dogtooth to syntaxial cements (FDC), microsparitic ferroan geopetal cements (MFGC), brown-luminescent banded dogtooth cements (BLBDC), blocky calcite cementation (BC), microsparitic non-ferroan geopetal cements (MNFGC). The line inside the box is the median, and the top and base of the box correspond to the quartiles. Ninety per cent of the values are between the upper and lower boundaries, and the points correspond to the values outside this interval.

values (median: −4·5‰; $n = 13$) would imply seawater temperatures of at least 50°C, which is very unlikely. The cloudy orange to brown luminescence also suggests transformation of fibrous cement initially with an unstable mineralogy into low-magnesium calcite (Durlet & Loreau, 1996; Loreau & Durlet, 1999; Knoerich & Mutti, 2003; Richter *et al.*, 2003). The slightly negative $\delta^{13}C$ signal of this cement, with a median value of −1·3‰, could mark the circulation of ^{12}C enriched meteoric fluids during burial (Derry, 2010). Isopachous fibrous cements are ferroan (median: 0·55% $FeCO_3$), like blocky calcite in the FAY11 sample (median: 0·67% $FeCO_3$), indicating stabilization in a reduced environment, where Fe^{2+} is free and can be incorporated within the crystal lattice.

The $\delta^{18}O$ signal found for isopachous fibrous cements is in the range of the analyses already performed by authors on recrystallized fibrous cements (Tobin *et al.*, 1996; Christ *et al.*, 2012a; Dickson & Kenter, 2014).

High-resolution $\delta^{18}O$ variation within pendant cements

The pendant cements studied are similar to those described by Purser (1969) from the Bathonian of the Burgundy platform which were interpreted as being vadose in origin. Pendant cements display negative $\delta^{18}O$ values ranging from −6·6 to −1·9‰ (median: −4·1‰) and mainly positive $\delta^{13}C$ values fluctuating between −1·1‰ and +4·9‰ (median: +0·8‰; Fig. 10B). These values are of the same order of magnitude as values obtained by microdrilling on similar Bathonian pendant cements from the eastern Paris Basin by Brigaud *et al.* (2014b); $\delta^{18}O$ from −6 to −2‰ and $\delta^{13}C$ from +2·2 to +5·6‰. However, $\delta^{18}O$ values are more heterogeneous within individual pendant cements than previously expected. The cements are characterized by an alternation between slightly blue luminescent limpid zones that precipitated in meteoric water (median $\delta^{18}O$: −4·1‰; $n = 10$) and pink-orange luminescent fibrous crystals that precipitated in

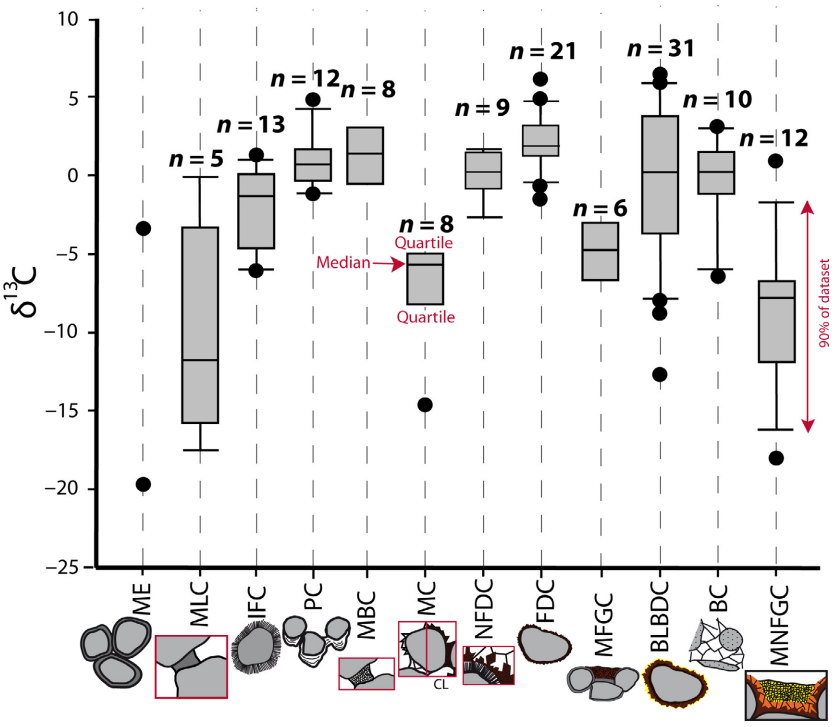

Fig. 8. $\delta^{13}C$ (‰-PDB) of the different cement types: micritic envelopes (ME), meniscus-like cements (MLC; *sensu* Hillgärtner *et al.*, 2001), isopachous fibrous cements (IFC), pendant cement (PC), microsparitic bridge cements (MBC), meniscus cements (MC), non-ferroan dogtooth to syntaxial cements (NFDC), ferroan dogtooth to syntaxial cements (FDC), microsparitic ferroan geopetal cements (MFGC), brown-luminescent banded dogtooth cements (BLBDC), blocky calcite cementation (BC), microsparitic non-ferroan geopetal cements (MNFGC). The line inside the box is the median, and the top and base of the box correspond to the quartiles. Ninety per cent of the values are between the upper and lower boundaries and the points correspond to the values outside this interval.

marine to mixed water ($\delta^{18}O$ values are −2·5‰ and −1·9‰; n = 2; Figs 10B, 13A and 17B). Pendant cements developed in a supratidal setting (vadose zone) near the coastline (Fig. 18). Contrary to isopachous fibrous cements, the marine $\delta^{18}O$ signature of pendant fibrous cements indicates an initial low-magnesium calcite mineralogy (Fig. 17B). No mineralogical transformation of calcite occurred during burial diagenesis. The two narrow pink-luminescent bands indicate two stages of marine water input that cannot be evidenced by classical analytic methods and allow a more precise characterization of the precipitation environment.

Sparitic meniscus cements and microsparitic bridge cements: a different palaeoenvironmental significance

Meniscus cements are commonly used to characterize exposure surfaces because they are described by authors as being indicative of marine to meteoric vadose environments (Purser, 1969; Longman, 1980; Christ *et al.*, 2015). However, they have to be identified very carefully to avoid any confusion. The shape of microsparitic bridges, for example, makes it tempting to interpret these cements as forming in the vadose zone, similarly to sparitic meniscus cements. The $\delta^{13}C$ and $\delta^{18}O$ values of these two types of cement had never been characterized before because of their small size.

The negative $\delta^{18}O$ values (−5·5 to −3·6‰; median: −4·3‰) of meniscus cements (Figs 13D and 14) are typical of precipitation in meteoric water (Fig. 17D), and their very negative $\delta^{13}C$ values (−14·8 to −4·4‰; median: −5·5‰) mark the percolation of fluids through an organic-rich soil horizon and their enrichment in ^{12}C (Godet *et al.*, 2016). Sparitic meniscus cements formed in the vadose meteoric zone, in a supratidal to continental setting below a soil horizon (Fig. 18). The variability of the $\delta^{13}C$ signature, clearly lower than for brown-luminescent banded dogtooth cements, indicates varying enrichment of the parent fluid in organic carbon

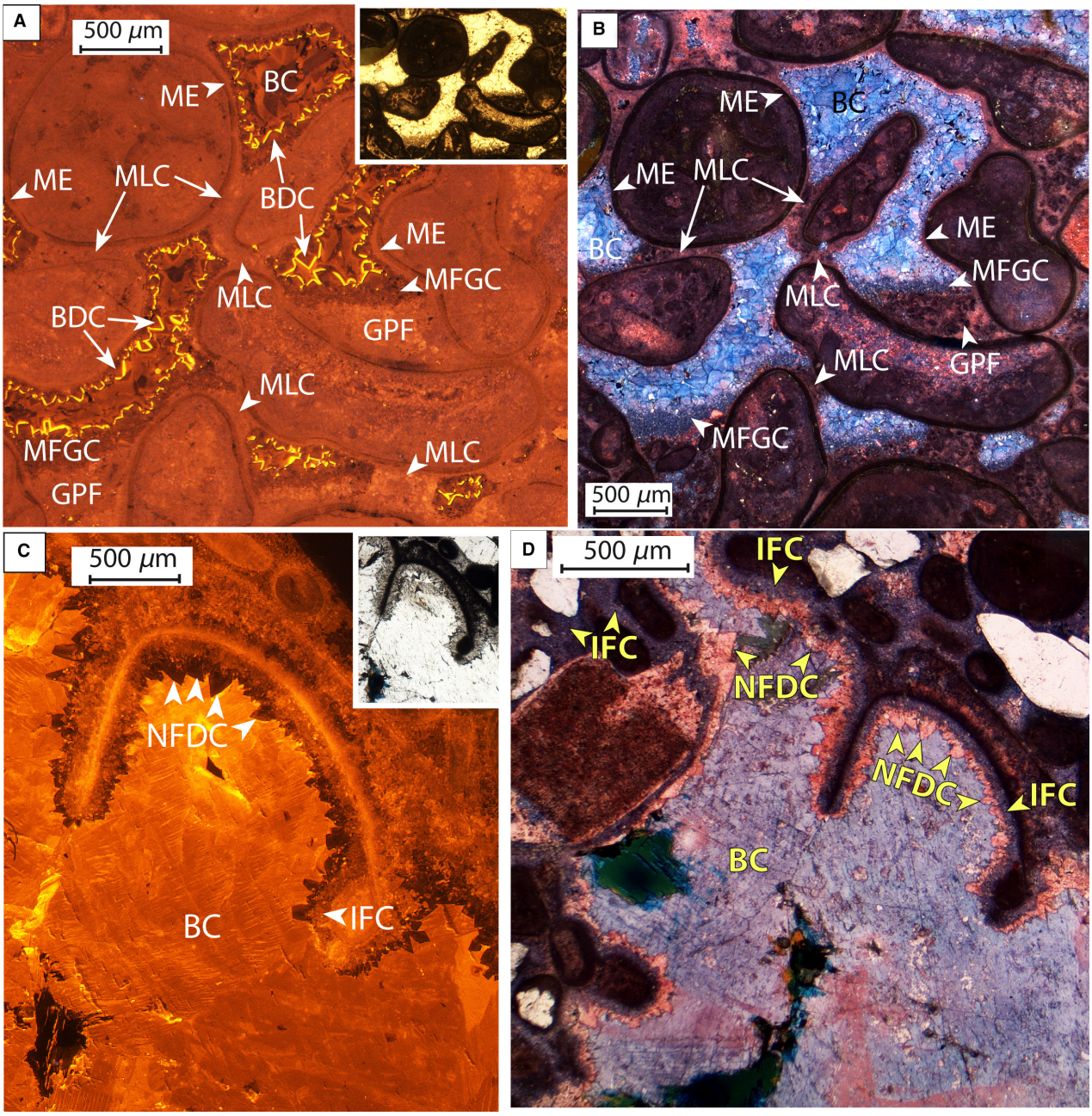

Fig. 9. Thin-section Au4, Site 2, sequence boundary Bt2, Calcaire de Blainville Formation, Bathonian. (A) Cathodoluminescence (CL) image of a bioclastic to oolitic grainstone displaying ME, MLC (*sensu* Hillgärtner *et al.*, 2001), GPF, MFGC, BLBDC and BC. (B) Alizarin–potassium ferricyanide stained view of a bioclastic to oolitic grainstone displaying ME, MLC (*sensu* Hillgärtner *et al.*, 2001), GPF, MFGC, BLBDC and BC. FAY11, Site 1, sequence boundary Bj1, Sables et Graviers de Tessé Formation, Aalenian. (C) CL image of IFC, FDC and BC. (D) Alizarin–potassium ferricyanide stained view of IFC, FDC and BC. ME, micritic envelopes; MLC, meniscus-like cements; GPF, geopetal peloidal fabric; MFGC, microsparitic ferroan geopetal cements; BLBDC, brown-luminescent banded dogtooth cements; BC, blocky calcite; IFC, isopachous fibrous cements; FDC, ferroan dogtooth to syntaxial cements.

that may result from changing amounts of organic matter in the soil horizon.

The $\delta^{18}O$ value (median: −1·7‰) of non-luminescent and ferroan ($FeCO_3$ molar percentages: 0·12% and 0·3%) low-magnesium calcite microsparitic bridge cements (Fig. 13B and C) indicates precipitation in marine to mixed or meteoric water, as the most negative

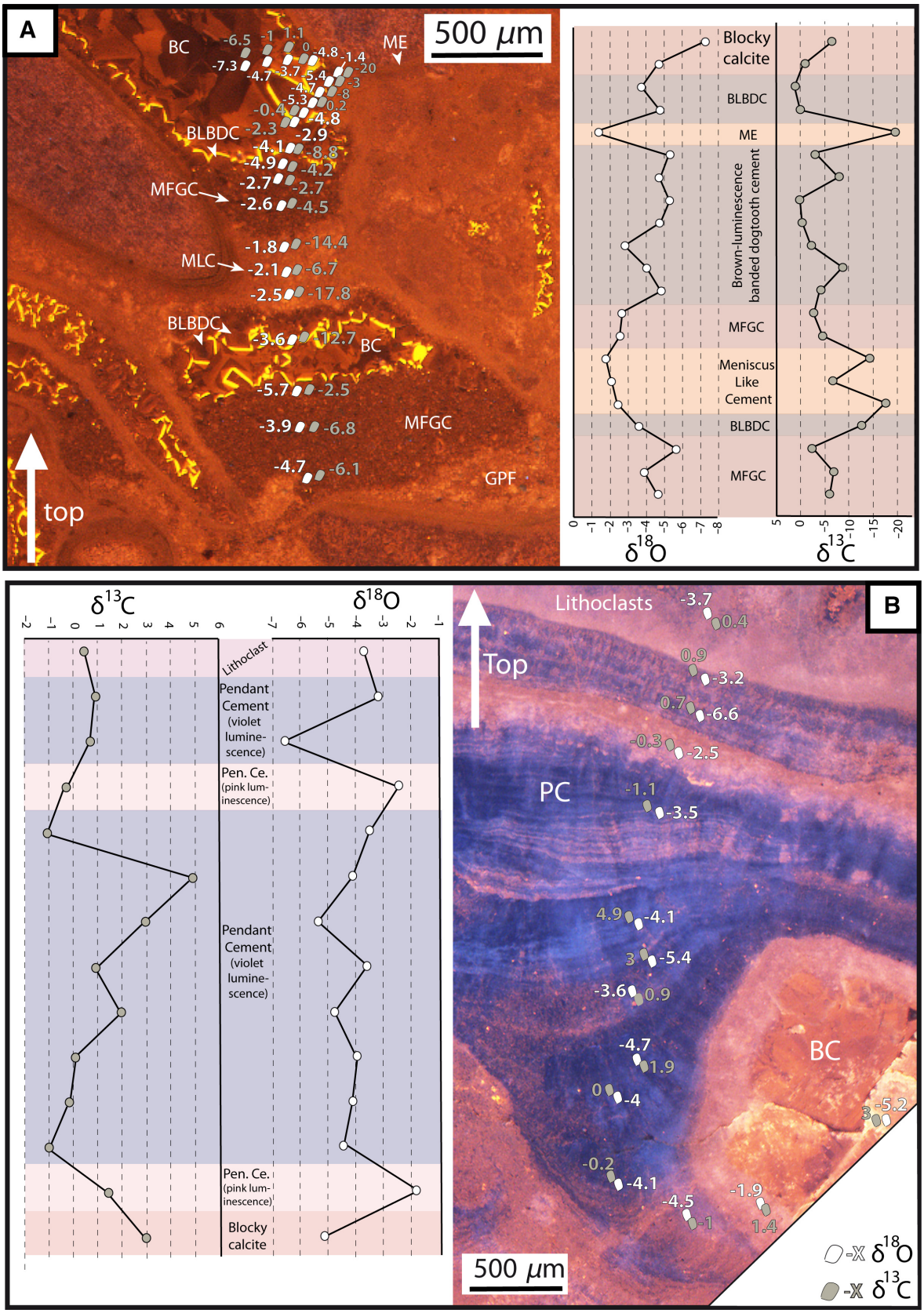

Fig. 10. Cathodoluminescence (CL) image of detailed SIMS transects performed on thin sections AU4 and EST 436, showing $\delta^{18}O$ and $\delta^{13}C$ (‰-PDB) variability. (A)Thin-section AU4 – GPF, ME, MLC, MFGC, BLBDC and BC. (B) Thin-section EST 436 – PC and BC. GPF, geopetal peloidal fabric; ME, micritic envelopes; MLC, meniscus-like cements; MFGC, microsparitic ferroan geopetal cements; BLBDC, brown-luminescent banded dogtooth cements; BC, blocky calcite; PC, pendant cement.

value reaches −4·1‰ (Fig. 17C). Their $\delta^{13}C$ displays a clearly marine signature (median: +1·7‰) despite a quite high variability from −0·9‰ to +4·2‰. This variability could result from local modifications of the microenvironments and associated $\delta^{13}C$ of the seawater. For example, moderate microbial activity could locally lower the carbon isotope composition of the seawater. The particular morphology of these cements, forming elongate bridges or patch filling porosity, is different from classical sparitic meniscus cements with concave borders, indicative of vadose diagenesis (Purser, 1969; Longman, 1980; Christ *et al.*, 2015), and makes it unlikely that they formed by capillary forces. Moreover, microsparitic bridges formed in association with marine ferroan dogtooth cements, precipitating in the marine phreatic zone. A microbial origin should be considered for these cements because they display similar morphology and size to some meniscus-like cements (100 to 500 μm long elongated micrite bridges between grains; Hillgärtner *et al.*, 2001) and formed in

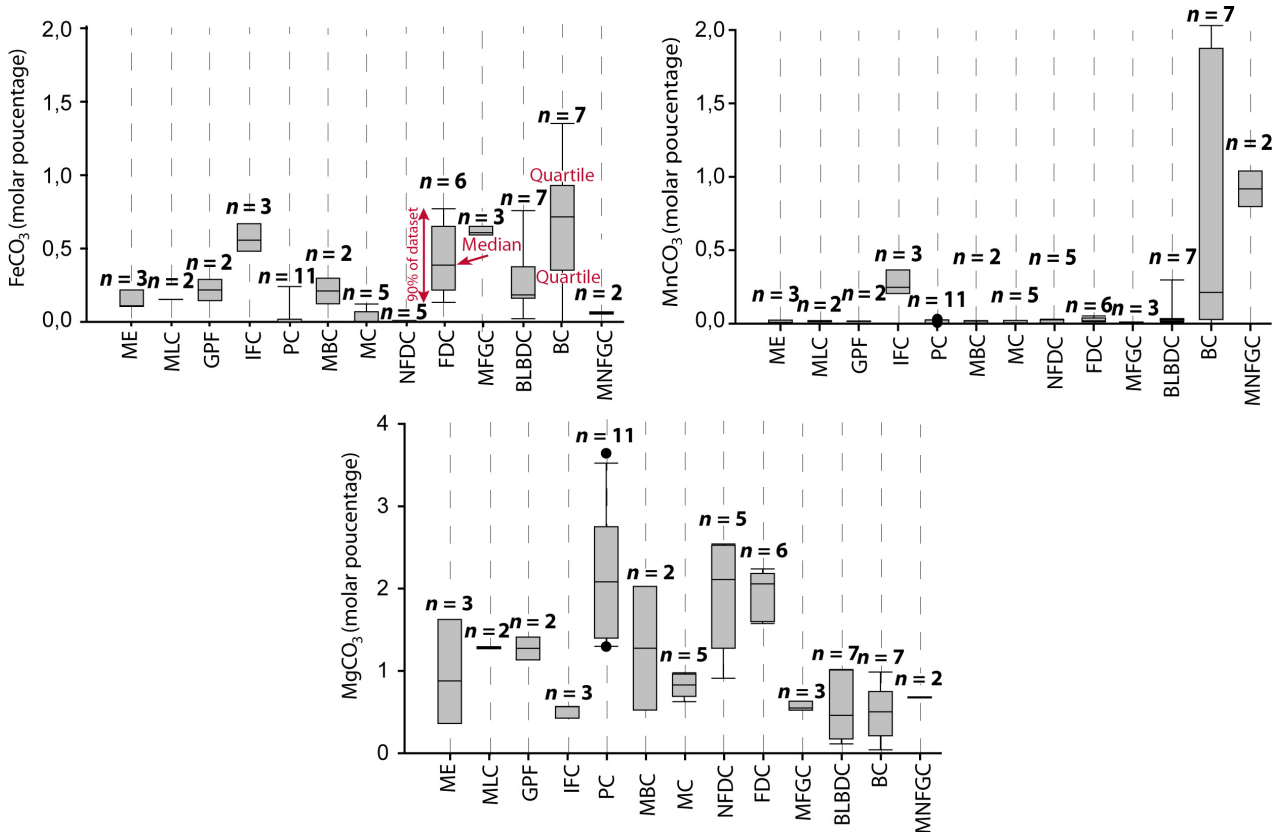

Fig. 11. Molar percentages of $FeCO_3$, $MnCO_3$ and $MgCO_3$ within the different cement types: micritic envelopes (ME), meniscus-like cements (MLC; *sensu* Hillgärtner *et al.*, 2001), geopetal peloidal fabric (GPF), isopachous fibrous cements (IFC), pendant cement (PC), microsparitic bridge cements (MBC), meniscus cements (MC), non-ferroan dogtooth to syntaxial cements (NFDC), ferroan dogtooth to syntaxial cements (FDC), microsparitic ferroan geopetal cements (MFGC), brown-luminescent banded dogtooth cements (BLBDC), blocky calcite cementation (BC) and microsparitic non-ferroan geopetal cements (MNFGC). The line inside the box is the median, and the top and base of the box correspond to the quartiles. Ninety per cent of the values are between the upper and lower boundaries and the points correspond to the values outside this interval.

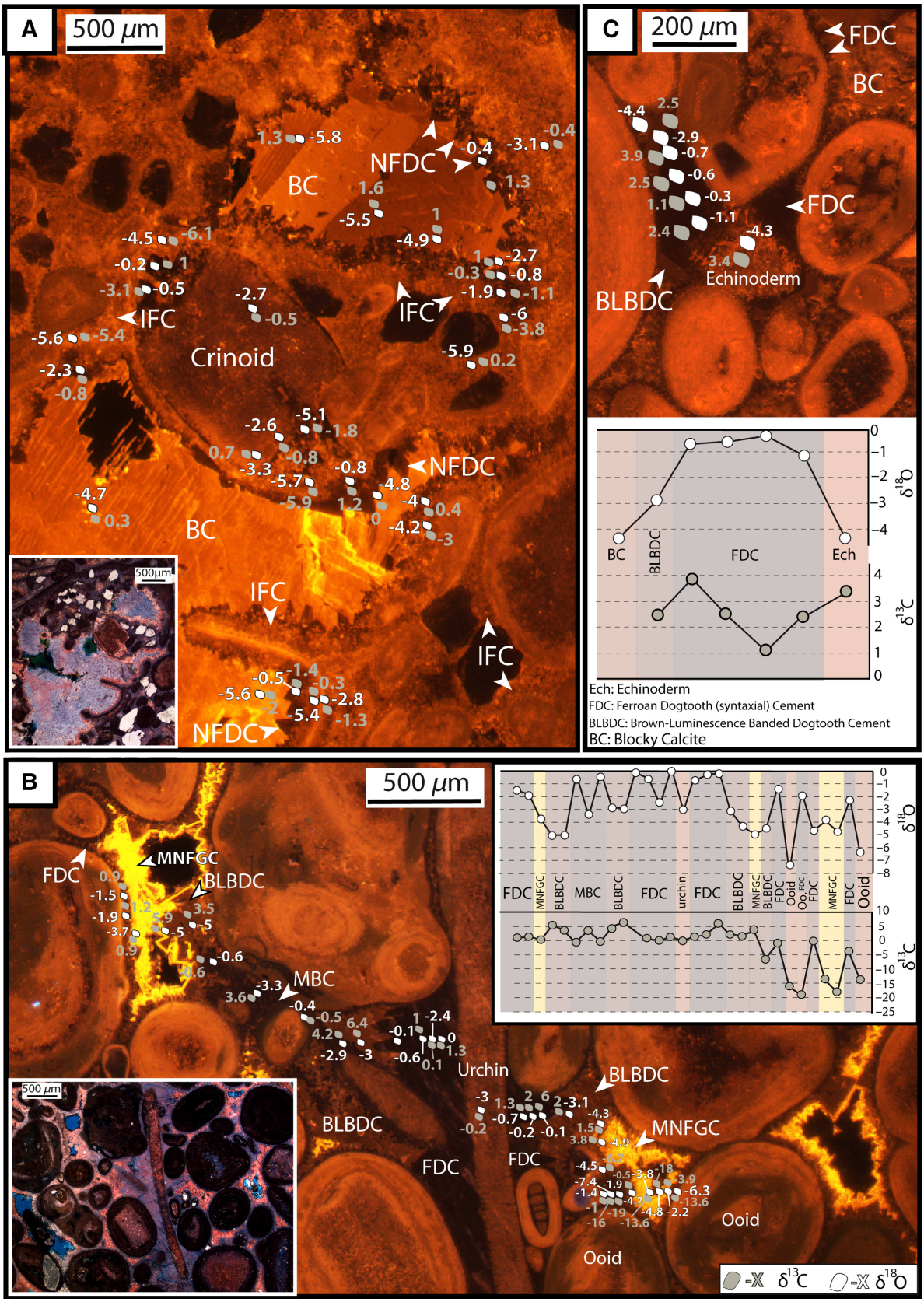

Fig. 12. Cathodoluminescence (CL) image of detailed SIMS transects performed in thin-section FAY11, showing the $\delta^{18}O$ and $\delta^{13}C$ (‰-PDB) variability. (A) Isopachous fibrous cement (IFC), non-ferroan dogtooth to syntaxial cement (NFDC) – VSH10. (B) Ferroan dogtooth to syntaxial cement (FDC), brown-luminescent banded dogtooth cements (BLBDC), microsparitic bridge cements (MBC) and microsparitic non-ferroan geopetal cement (MNFGC) – with associated $\delta^{18}O$ and $\delta^{13}O$ values. (C) Ferroan dogtooth to syntaxial cement (FDC), brown-luminescent banded dogtooth cements (BLBDC) and blocky calcite (BC).

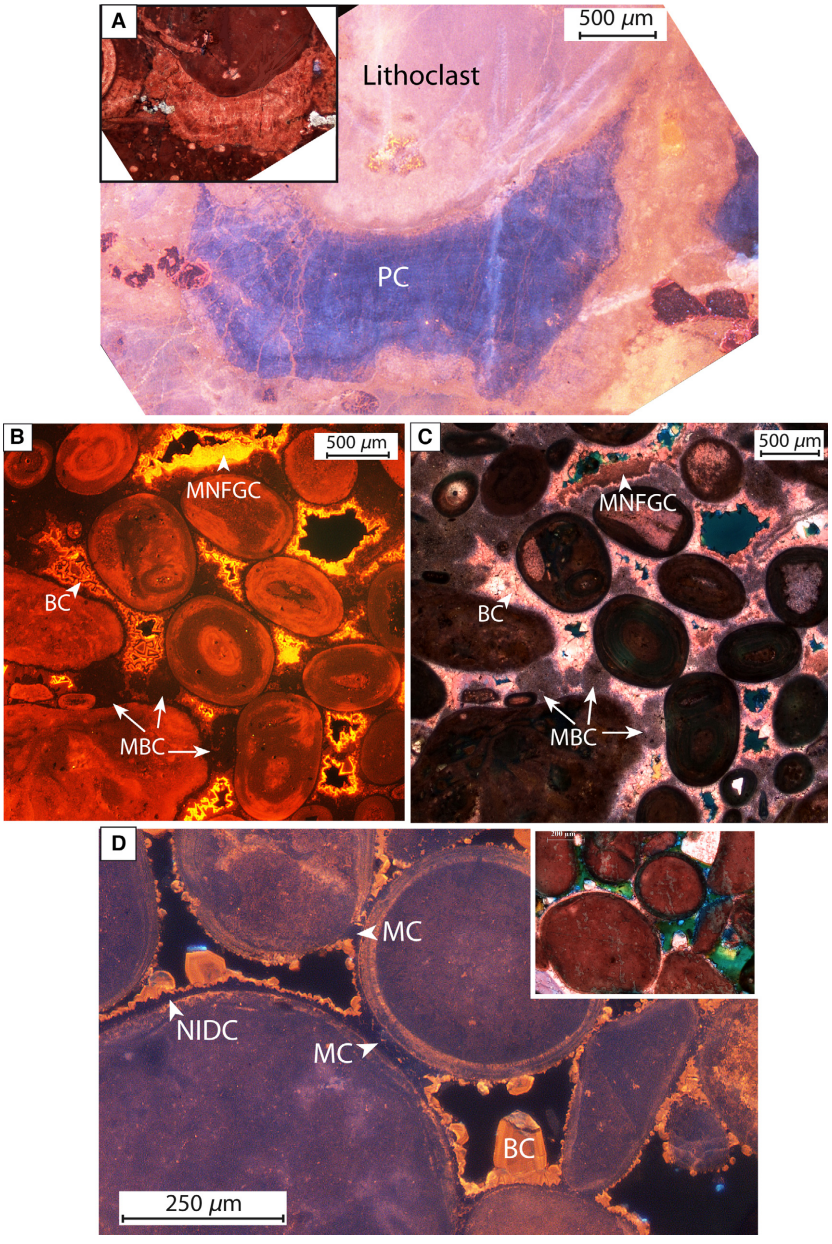

Fig. 13. (A) Cathodoluminescence (CL) image of thin-section E436, Site 3, sequence boundary Bt2, Calcaires de Chaumont Formation, Bathonian, showing pendant cements (PC). Thin-section VSH6, Site 1, sequence boundary Ox1, Calcaire corallien de Mortagne Formation, Oxfordian. (B) CL view of an oolitic to lithoclastic grainstone with numerous MBC and MNFGC following BC. (C) Alizarin–potassium ferricyanide stained view of an oolitic to lithoclastic grainstone with numerous MBC and MNFGC following BC. Thin-section E409, Site 3, sequence boundary Bt4, Oolithe de Fréville Formation, Bathonian. (D) CL image of an oolitic grainstone with numerous MC and BC. MBC, microsparitic bridge cements; MNFGC, microsparitic non-ferroan geopetal cements; BC, blocky calcite; MC, meniscus cements.

reducing environments, as indicated by the incorporation of Fe^{2+} (Léonide *et al.*, 2012). The mechanism of formation of microsparitic bridge cements is difficult to define, but they probably formed in a subtidal to intertidal setting in this case. Microsparitic bridge cements should therefore not be considered alone as indicative of vadose diagenesis (Fig. 18).

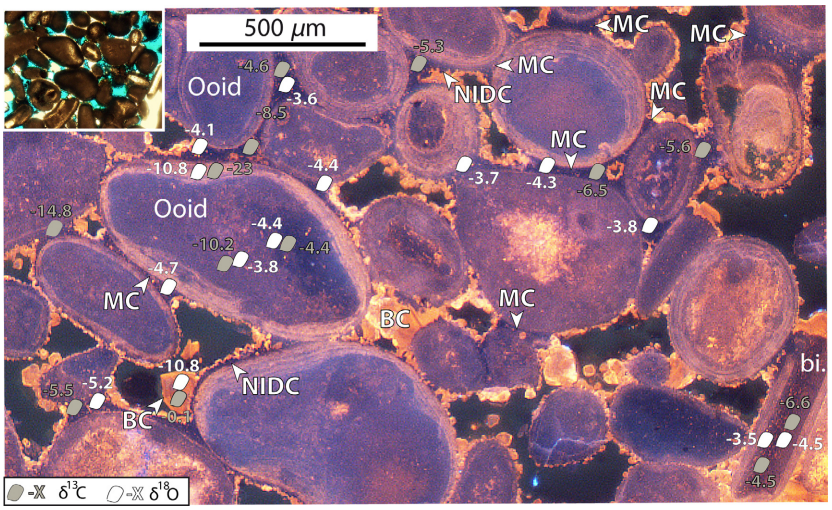

Fig. 14. Cathodoluminescence (CL) image of a detailed SIMS transect performed on thin-section EST409, showing the $\delta^{18}O$ and $\delta^{13}C$ (‰-PDB) variability – meniscus cement (MC), non-isopachous dogtooth cement (NIDC) and blocky calcite (BC) – with the associated $\delta^{18}O$ and $\delta^{13}O$ values.

Variability of $\delta^{18}O$ and $\delta^{13}C$ signals between different dogtooth cements: linking palaeoenvironments to chemical properties

Dogtooth calcite is recognized in a wide variety of environments from the meteoric to the shallow burial realm and is also known from marine and hydrothermal settings (Durlet & Loreau, 1996; Flügel, 2010; Christ *et al.*, 2015). Here, the variability in $\delta^{18}O$ and $\delta^{13}C$ signals of four dogtooth cements is documented. Marine and non-marine phreatic dogtooth cements display different luminescence and alizarin–potassium ferricyanide staining, which could be used in the future for their palaeoenvironmental characterization.

The $\delta^{18}O$ and $\delta^{13}C$ signals in isopachous non-ferroan dogtooth cements (NFDC; median: −0·8‰ for $\delta^{18}O$ and +1‰ for $\delta^{13}C$; Fig. 9C to D) and ferroan dogtooth cements (FDC; median: −0·7‰ for $\delta^{18}O$ and +1·6‰ for $\delta^{13}C$; Figs 15 and 16) are clearly characteristic of precipitation in marine water (Fig. 17E and F) in the phreatic zone (subtidal environment; Fig. 18). They have original low-magnesium calcite mineralogy, as attested to by their limpid, non-luminescent crystals (Durlet & Loreau, 1996; Loreau & Durlet, 1999). Non-ferroan cements formed in oxidizing water, while ferroan cements are characteristic of reducing conditions (Mallarino *et al.*, 2002; Léonide *et al.*, 2012). Their sizes differ significantly, varying between about 20 μm long for ferroan dogtooth cements and 20 to 200 μm long for non-ferroan dogtooth cements. Isotopic data reveal that, if the $\delta^{18}O$ does not show a very large variability, the $\delta^{13}C$ is very variable within these cements. The amplitudes of the variations of carbon isotope composition values are 5·4‰ and 6·5‰ for non-ferroan and ferroan dogtooth cements, respectively. This is the first time that such a disparity of the $\delta^{13}C$ signature is evidenced in marine dogtooth cements. The origin of this variability is difficult to interpret but could result from very local modifications of the microenvironments.

Non-isopachous dogtooth crystals (NIDC; Figs 13D and 14) formed together with sparitic meniscus cements (MC) and formed in the vadose meteoric zone, in a supratidal setting under a soil horizon (Fig. 18). Vadose non-isopachous dogtooth cements and marine non-ferroan dogtooth cements both form in oxidizing environments and so display similar CL and alizarin–potassium ferricyanide staining (low $FeCO_3$ and $MnCO_3$ molar percentages). The vadose dogtooth cements do not develop continuously all around the grains (non-isopachous)

Fig. 15. Thin-section VSH10 – Site 1, sequence boundary Ox1, Calcaire corallien de Mortagne Formation, Oxfordian. (A) Cathodoluminescence (CL) image of an oolitic grainstone with FDC and BC. (B) Alizarin–potassium ferricyanide stained view of an oolitic grainstone with FDC and BC. Thin-section VSH6 – Site 1, sequence boundary Ox1, Calcaire corallien de Mortagne Formation, Oxfordian. (C) CL image of an oolitic grainstone with FDC, BLBDC and MNFGC. (D) Alizarin–potassium ferricyanide stained view of an oolitic grainstone with FDC, BLBDC and MNFGC. FDC, ferroan dogtooth to syntaxial cements; BC, blocky calcite; BLBDC, brown-luminescent banded dogtooth cements; MNFGC, microsparitic non-ferroan geopetal cements.

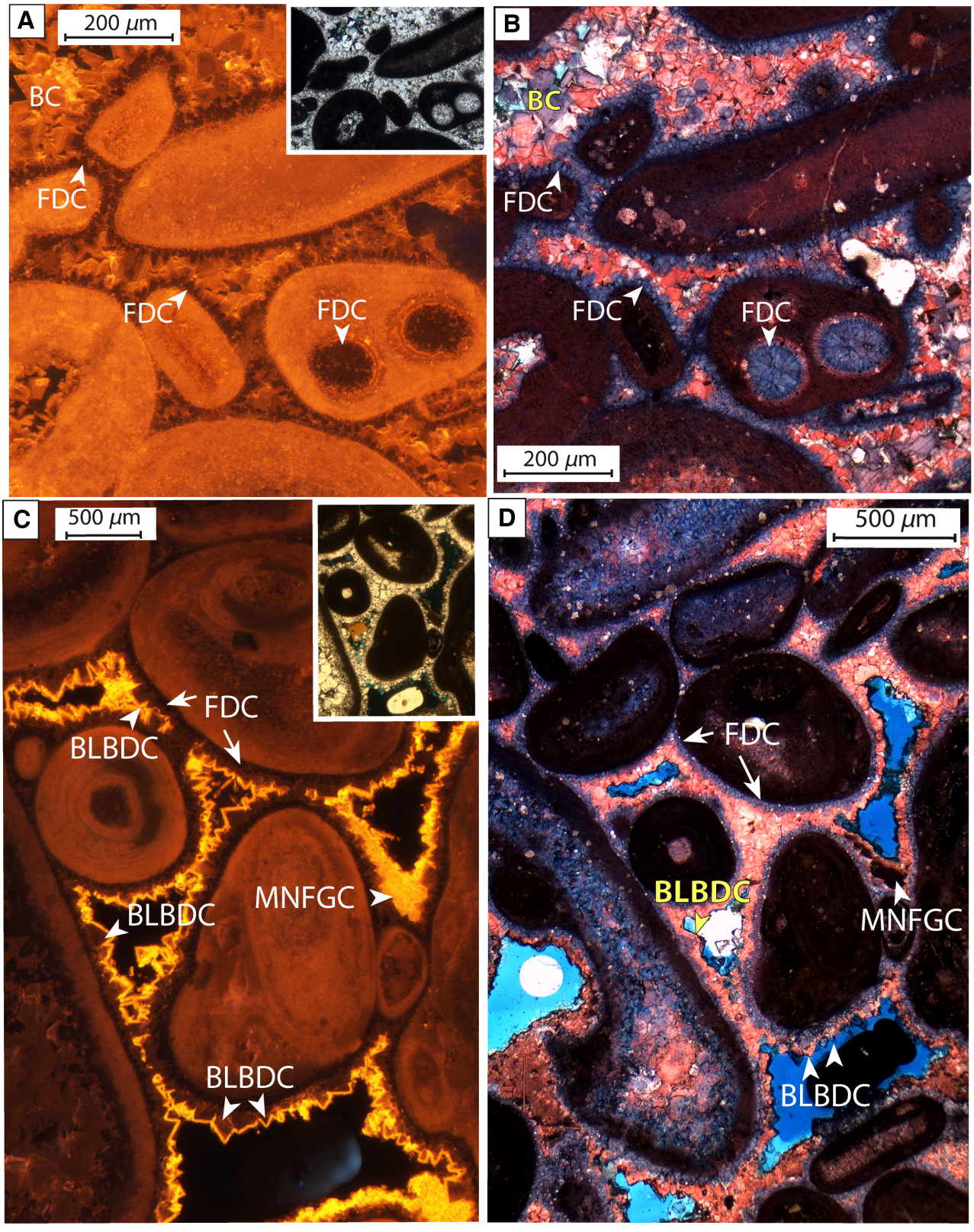

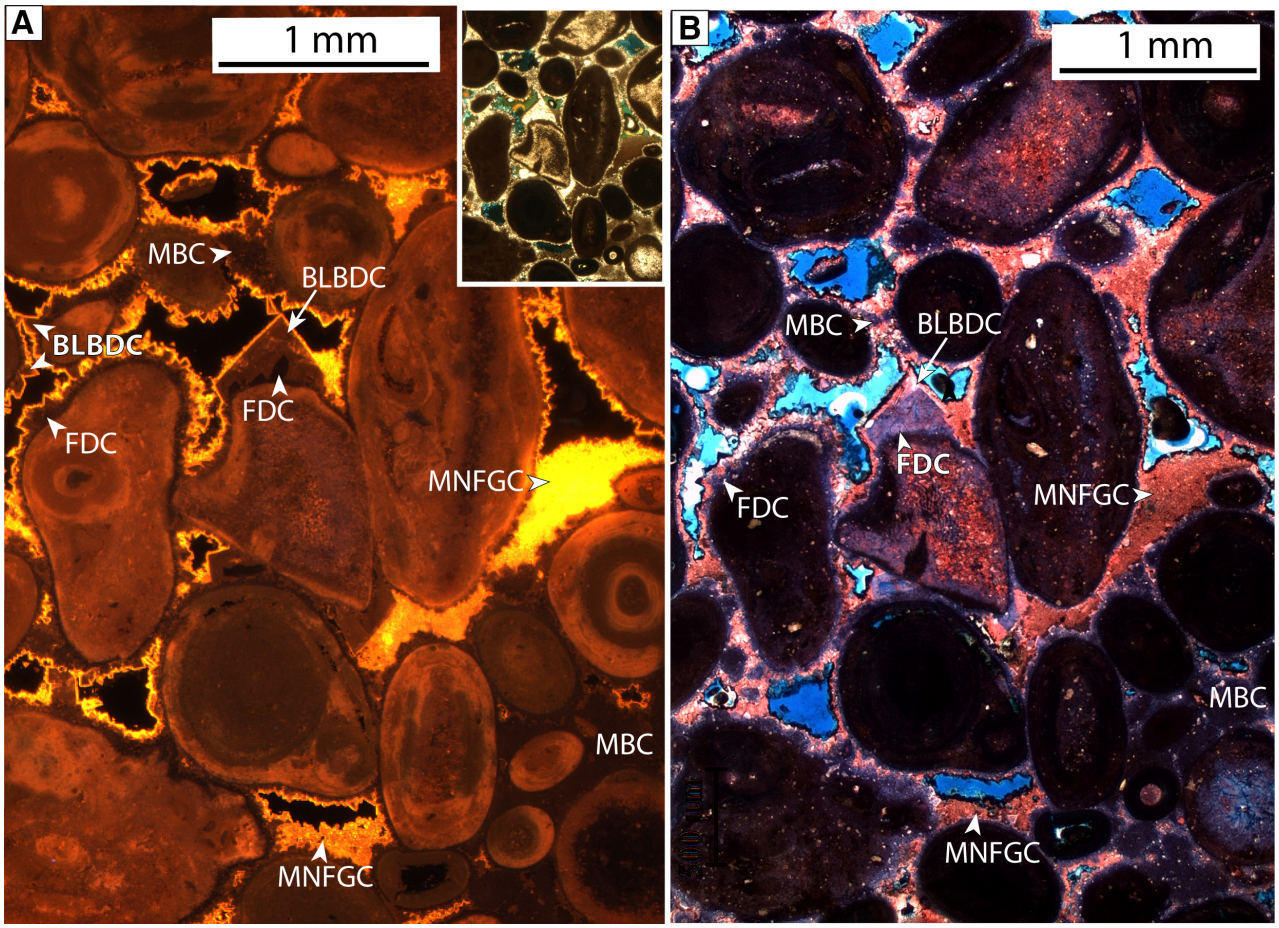

Fig. 16. Thin-section VSH6 – Site 1, sequence boundary Ox1, Calcaire corallien de Mortagne Formation, Oxfordian. (A) Cathodoluminescence (CL) image of an oolitic to lithoclastic grainstone with FDC, MBC, BLBDC and MNFGC. (B) Alizarin–potassium ferricyanide stained view of an oolitic to lithoclastic grainstone with FDC, MBC, BLBDC and MNFGC. FDC, ferroan dogtooth to syntaxial cements; MBC, microsparitic bridge cements; BLBDC, brown-luminescent banded dogtooth cements; MNFGC, microsparitic non-ferroan geopetal cements.

and are associated with clear meniscus cements (Fig. 14).

The last dogtooth cement type identified corresponds to brown-luminescent dogtooth crystals (BLBDC) surrounded by a narrow, bright yellow/orange luminescent band (Figs 15C, 15D and 16). They exhibit variable molar percentages of $FeCO_3$ (0·02 to 0·75%) and light $\delta^{18}O$ signature about −4·5‰ that could result from precipitation: (i) from meteoric water (Fig. 17H); or (ii) from marine fluids heated (at least 50°C) during burial (Tobin *et al.*, 1996). However, coarser blocky calcite crystals post-date the brown-luminescent dogtooth crystals and have significantly more negative $\delta^{18}O$ than the brown-luminescent banded dogtooth cements, varying from −4·7 to −10·8‰ (median: −5·6‰). Banded dogtooth cements described by Godet *et al.* (2016), with mean $\delta^{13}C$ of −1·3‰ and $\delta^{18}O$ of −5·2‰, were attributed to meteoric diagenesis, especially because of their variable luminescence (dull to bright) and $FeCO_3$ and $MnCO_3$ molar percentages, characterizing changes from reducing to oxidizing fluids (Budd *et al.*, 2000; Léonide *et al.*, 2012). The latter, the very variable and negative $\delta^{13}C$ values, as well as the isopachous fabric of brown-luminescent banded dogtooth cements from −12·7‰ to +6·4‰ suggest precipitation below a soil horizon in the meteoric water zone during early diagenesis (Fig. 18; Godet *et al.*, 2016). The banded dogtooth cements can be petrographically differentiated from marine phreatic dogtooth cements based on the intensity of their luminescence and alizarin–potassium ferricyanide staining colours. The very high variability of the $\delta^{13}C$ signature (amplitude: 17·1‰)

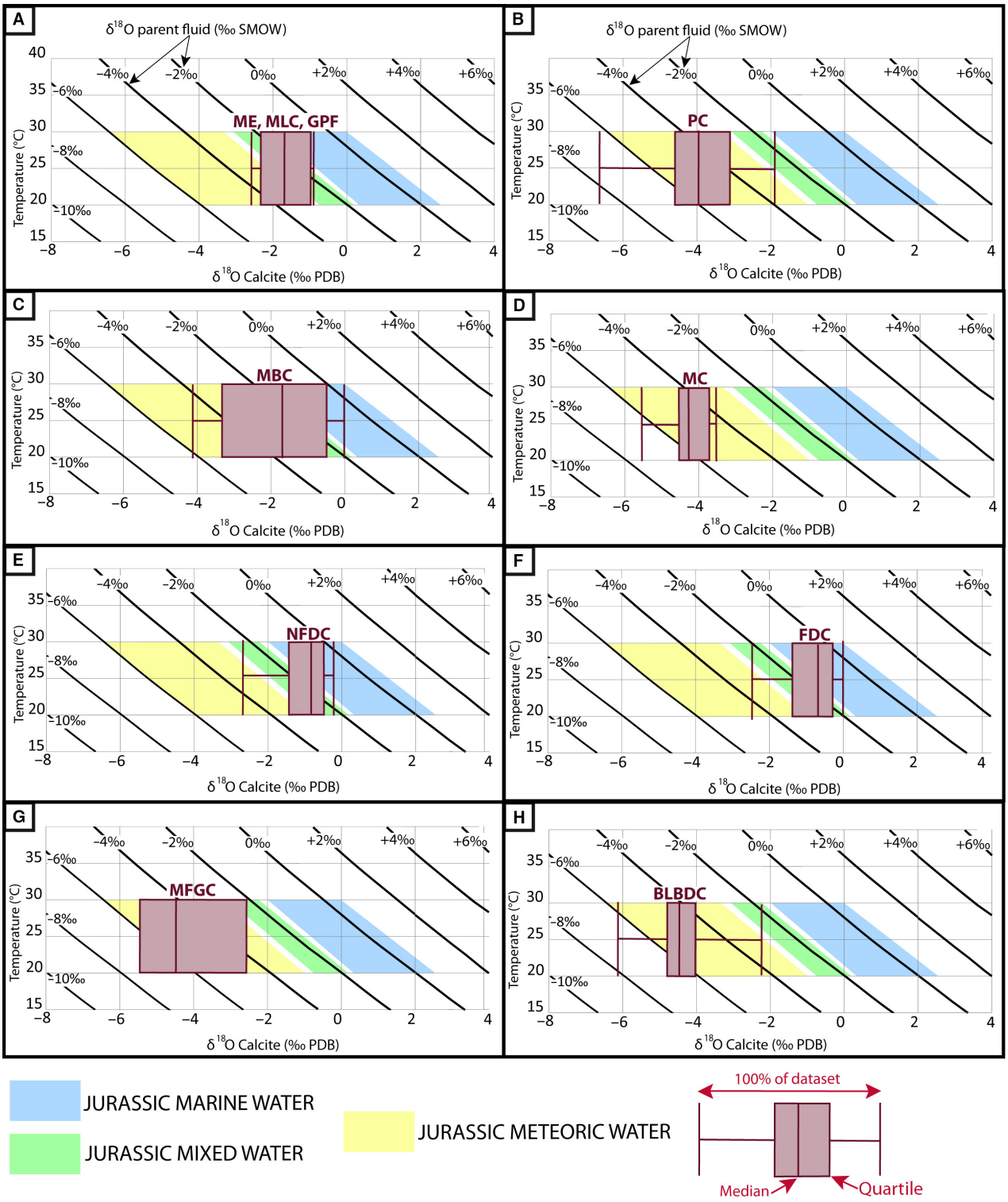

Fig. 17. Box (median ± standard deviation) of the δ^{18}O PDB of the early cement stages plotted on a fractionation diagram between temperature and δ^{18}O PDB of calcite reconstructed with the equation of Zheng (1999). (A) Micritic fabrics (micritic envelopes, meniscus-like cements and peloidal geopetal cements). (B) Pendant cements. (C) Microsparitic bridge cements. (D) Meniscus cements. (E) Non-ferroan dogtooth cements. (F) Ferroan dogtooth cements. (G) Microsparitic ferroan geopetal cements. (H) Brown-luminescent banded dogtooth cements.

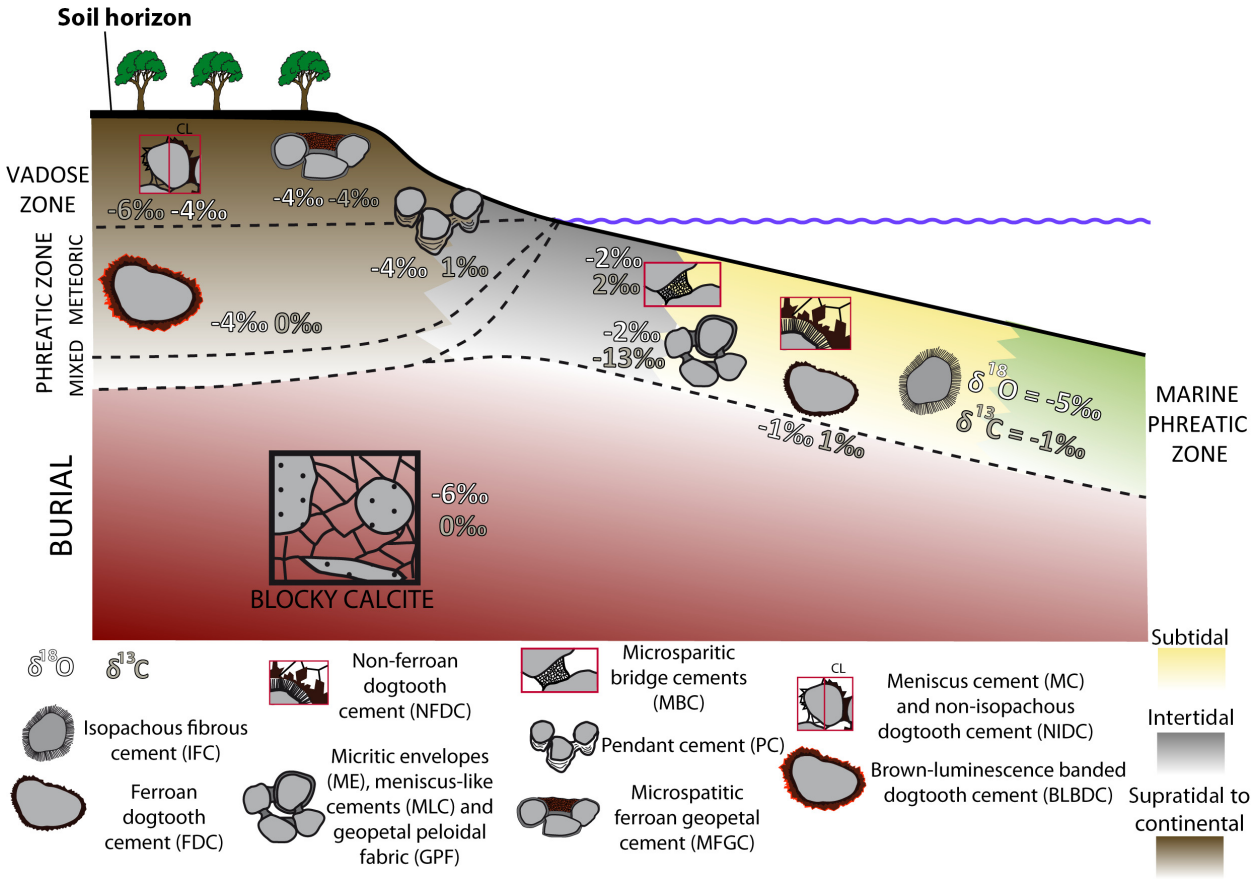

Fig. 18. Location of the early and burial cements studied, in their environments of formation on a carbonate platform cross-section from the upper offshore to the backshore.

within these cements indicates a differential enrichment in organic carbon. This feature can be the consequence of: (i) a variation over time of the abundance of organic matter within the soil horizon; and/or of (ii) the fact that the soil cover was not permanent. The $\delta^{18}O$ signature is also marked by a large variability (−6·1 to −2·2‰; amplitude: 3·9‰) that may partially result from modifications of the temperature of meteoric water, possibly related to seasonal changes. A temperature change of about 16°C is necessary to explain a 4‰ variation of the $\delta^{18}O$ signature of calcite (Fig. 17).

Geopetal cements: an eogenetic to telogenetic timing of formation

The $\delta^{18}O$ and $\delta^{13}C$ signatures in geopetal microsparitic cements can be used to differentiate between two geopetal cement types formed at different times in different environments. The two types can be distinguished by their luminescence and alizarin–potassium ferricyanide staining patterns.

The formation of microsparitic ferroan geopetal cements precedes the development of brown-luminescent banded cements (Figs 9A, 9B and 10A). These cements display negative $\delta^{18}O$ values (median: −4·3‰) that confirm their precipitation from meteoric water (Fig. 17G). Their very light $\delta^{13}C$ (median: −4·4‰) certainly has an organic-rich soil horizon as its origin. The $\delta^{13}C$ values, while variable (−2·7 to −6·8‰; amplitude: 4·1‰), are always negative, indicating that the soil horizon was probably permanent. Variations over time of the abundance of organic matter within the soil horizon explain the high variability of the $\delta^{13}C$ values. Microsparitic ferroan geopetal cements display brown luminescence, blue alizarin–potassium ferricyanide staining and a high $FeCO_3$ molar percentage attesting to a high Fe^{2+} content, characteristic of a reduced environment (Léonide *et al.*, 2012).

The oxygen and carbon isotope values from microsparitic ferroan geopetal fabrics suggest a supratidal environment of formation, within the vadose zone. This is consistent with the work of Aissaoui & Purser (1983) on the Jurassic limestones of Burgundy, where geopetal microsparitic cements were found in association with microstalactitic cements, erosion surfaces and dissolution phenomena indicating the influence of meteoric water. Aissaoui & Purser (1983) proposed that geopetal microsparitic fabrics correspond to silt-sized grains produced by the erosion of a lithified substrate. Microsparitic ferroan geopetal cements display features (ferroan, meteoric $\delta^{18}O$ signature) that differ from earlier cement stages or from grains along discontinuity Bt2. Thus, they did not form from the erosion of substrate but rather precipitated directly in small meteoric water lenses forming during exposure.

Microsparitic non-ferroan geopetal cements have a similar morphology and crystal size as their ferroan counterparts (Fig. 16), while they formed later in the paragenetic sequence. They post-date brown-luminescent banded dogtooth cements and poorly developed blocky calcite that display very negative $\delta^{18}O$ values of around −9‰. In the Jurassic limestones of the Paris Basin, such a stable oxygen isotope signal of blocky calcite cements is typical of calcite precipitated during burial (Brigaud *et al.*, 2009b; Nader *et al.*, 2016). A Jurassic meteoric fluid of −6‰ SMOW must be heated to a minimum temperature of 40°C to generate a $\delta^{18}O$ of −9‰ in blocky calcite. Non-ferroan geopetal cements display higher $\delta^{18}O$ values, with a median value of −4·9‰. This 4‰ increase in $\delta^{18}O$ between blocky calcite and geopetal cements and the fact that they post-date the blocky calcite cements can be explained by: (i) exhumation of the surrounding rock leading to decreasing temperature during telogenesis; or (ii) a fluid evolution from meteoric to basinal fluids having gained their ^{18}O as a result of fluid/rock interaction during burial (Brigaud *et al.*, 2009b). The very bright luminescence and the high $MnCO_3$ molar percentage (median: 0·92%) of microsparitic non-ferroan geopetal cements indicate a high Mn^{2+} abundance, which is characteristic of moderately reduced environments (Eh = 0·2 to 0·8; Machel, 2000). The geopetal fabric of this cement indicates precipitation probably in a non-saturated or vadose zone, which is consistent with formation during the exhumation of the surrounding rocks. The variability of their $\delta^{18}O$ signal, from −6·0 to −3·7‰ (amplitude −2·3‰), could indicate changing temperatures of meteoric water. A temperature change of meteoric water of about 8°C is necessary to explain a 2‰ variation of the $\delta^{18}O$ signature of calcite (Fig. 17). The very light $\delta^{13}C$ values of non-ferroan geopetal cements (median: −7·8‰) could indicate: (i) the circulation of high pCO_2 fluids, enriched in ^{12}C, in a non-saturated zone during telogenesis (Derry, 2010); or (ii) the influence of an organic-rich soil horizon (Godet *et al.*, 2016). Nevertheless, note that the $\delta^{13}C$ displays a very important variability, from −13·6‰ to +0·9‰ (amplitude: 14·5‰), whose amplitude is quite higher than for the blocky calcite (9·5‰). This high variability of the $\delta^{13}C$ signatures in non-ferroan microsparitic geopetal cements indicates that fluids with differential enrichment in organic carbon, and thus different origins, circulated during the exhumation stage. The less negative $\delta^{13}C$ values could, for example, originate from precipitation in meteoric water that did not percolate through an organic-rich soil horizon.

Using early cements to classify lithified discontinuities in their palaeoenvironmental history

Morphology, fauna and facies are criteria used to classify different types of hardgrounds or exposure surfaces (Brett & Brookfield, 1984; Durlet & Loreau, 1996; Loreau & Durlet, 1999). Although less commonly used, early cement morphology and geochemistry record the palaeoenvironmental development of discontinuities and the timing of different events. This is useful, for example, in identifying composite surfaces that have undergone both marine and subaerial lithification (Loreau & Durlet, 1999). Here, five discontinuity types with different palaeoenvironmental histories are distinguished from the different samples studied, based on early cements and their geochemical signatures ($\delta^{13}C$, $\delta^{18}O$, Fe^{2+} and Mn^{2+}; Fig. 19).

Exposure surface 1

Exposure surface 1 is characterized by pendant cements with alternating limpid blue luminescent zones that precipitated in meteoric water and narrow fibrous pink-orange luminescent bands that precipitated in marine water. The mainly positive $\delta^{13}C$ values in both the blue and pink-luminescent areas (median: 0·8‰, from −1·1 to +4·9‰) do not indicate the presence of an organic-rich soil horizon which could have added organic carbon to the percolating meteoric

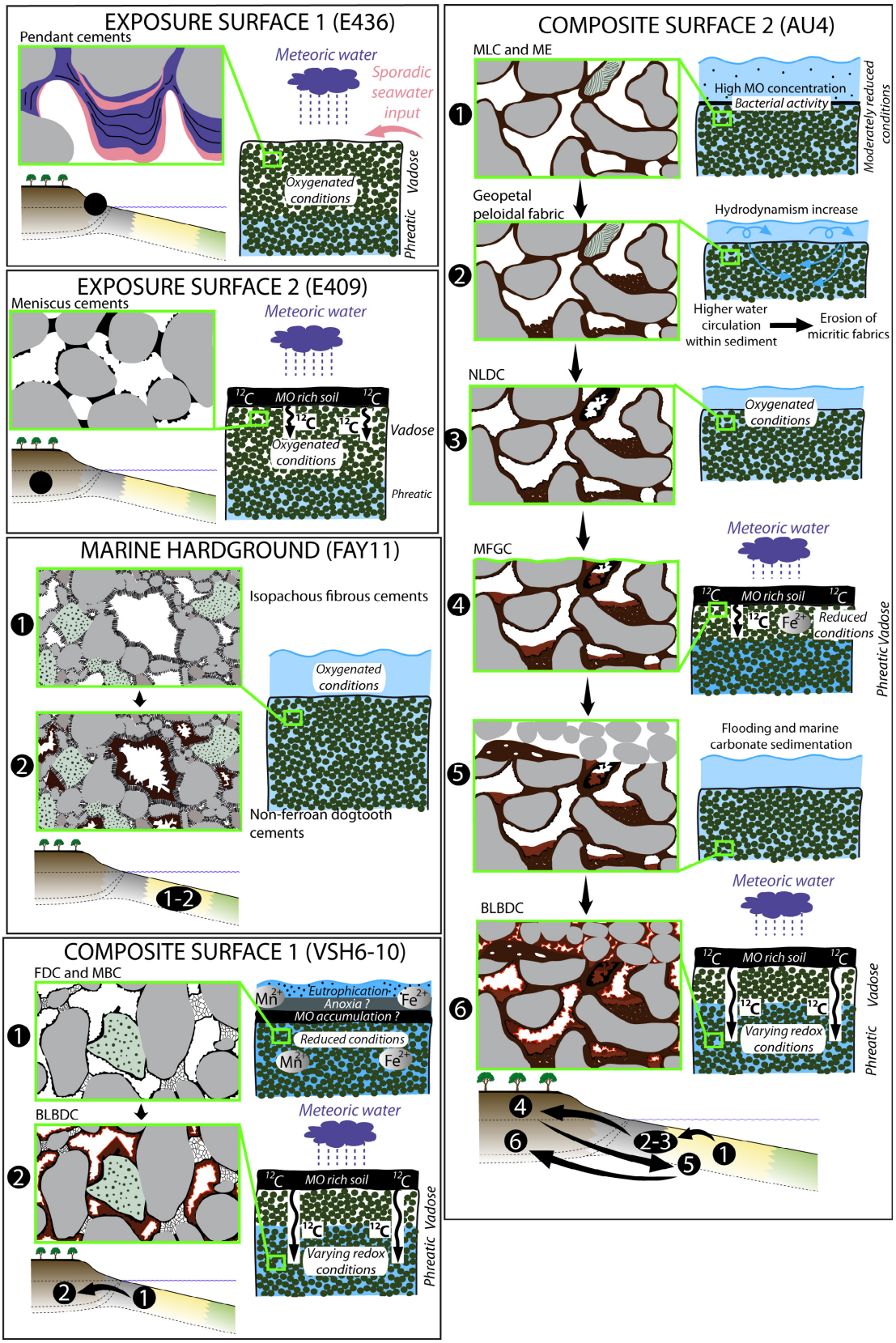

Fig. 19. Early carbonate cementation stages and related palaeoenvironmental evolution along five discontinuity types identified in the Jurassic limestones of the Paris Basin.

water from which the calcite precipitated (Godet *et al.*, 2016). Low amounts of Fe^{2+} (molar percentages of $FeCO_3$ from 0 to 0·26%) and Mn^{2+} (molar percentages of $MnCO_3$: 0%) indicate formation in oxidizing environments (Hendry *et al.*, 1995; Boggs & Krinsley, 2006; Fig. 19). In oxidizing water, iron, which is combined with oxygen and forms iron oxyhydroxides, cannot be incorporated within the calcite crystals, and Mn^{2+} ions are rare, inducing dull luminescence or non-luminescent features (Fig. 19; Machel, 1985; Major, 1991; Léonide *et al.*, 2012). Exposure surface 1 developed in a supratidal setting (vadose zone) near the coastline and marked by sporadic seawater inputs (Figs 18 and 19).

Exposure surface 2

Exposure surface 2 presents non-isopachous dogtooth and meniscus cements. Their low $\delta^{13}C$ and $\delta^{18}O$ values characterize precipitation in meteoric water below an organic-rich level, which is observed in cores (Figs 13 and 19; Godet *et al.*, 2016). The $FeCO_3$ and $MnCO_3$ molar percentages (0 to 0·02% for $MnCO_3$; 0·01 to 0·13% for $FeCO_3$) are indicative of oxidizing conditions. As the cements were sampled approximately 50 cm below the lignite layer, reduced conditions, that are often associated with organic matter, were probably only located in the first tens of centimetres below the lignite level, corresponding to a dark oolitic interval (Fig. 13). This surface type developed in the vadose zone and seems to characterize a more continental environment than exposure surface 1. This surface was probably not influenced by marine water input.

Marine hardground

From the marine hardgrounds Bj1 at Site 1, Bt4 at Site 2 and Bt3 at Site 3, only the marine hardground corresponding to discontinuity Bj1 at Site 1 has been analysed in detail, coupling petrographic description, ion microprobe and electron microprobe analyses (Fig. 19). Fibrous cements with a former high-magnesium calcite mineralogy are followed by low-magnesium calcite non-ferroan dogtooth cements, attesting to a clear change of calcite mineralogy. Electron microprobe analyses reveal a very low to negligible incorporation of both Mn^{2+} and Fe^{2+} in the calcite lattice (molar percentages range from 0 to 0·01% for $FeCO_3$ and 0 to 0·03% for $MnCO_3$) that is typical of seawater oxidizing conditions.

Composite surface 1

Composite surface 1 is marked by a first generation of ferroan non-luminescent dogtooth cements and microsparitic bridge marine cements (molar percentages of $FeCO_3$ from 0·13 to 0·77%; Fig. 19). Mallarino *et al.* (2002) and Léonide *et al.* (2012) describe similar early ferroan cements that they considered to have formed in reducing conditions, where Fe^{3+} is reduced to Fe^{2+} and can be incorporated within the calcite crystal lattice. The reduced conditions at the sea floor, and possible anoxia, were then attributed to high nutrient supply, eutrophication and local organic-matter burial (Mallarino *et al.*, 2002; Léonide *et al.*, 2012; Martinez & Dera, 2015; Andrieu *et al.*, 2016). The marine hardground after the formation of this first cement generation underwent exposure, leading to the growth of banded dogtooth cements. These cements formed in the meteoric vadose zone in various redox conditions and their low $\delta^{13}C$ characterizes the percolation of water through an organic-rich soil horizon.

Composite surface 2

Composite surface 2 displays a first stage of meniscus-like cements associated with micritic envelopes (Fig. 19). However, the orange luminescence, the near zero $MnCO_3$ amount and the moderate $FeCO_3$ molar percentage (0·11% for micritic envelopes and 0·15% for meniscus-like cements) do not suggest clearly reduced conditions in marine environments (Machel *et al.*, 1991; Machel, 2000).

The second diagenetic event recorded in the composite surface corresponds to the formation of geopetal peloidal fabrics. Their heavy $\delta^{18}O$ value of $-2{\cdot}4‰$ and very low $\delta^{13}C$ value of $-15‰$ ($n = 1$) suggest a microbially induced precipitation of peloids in marine water. These fabrics could have formed by erosion of micropeloidal meniscus-like cements by water, and then by filtering and deposition of the residual material (Aissaoui & Purser, 1983). They probably indicate increased hydrodynamism leading to greater water circulation within the sediment (Fig. 19). After the dissolution of aragonitic shells, marine non-ferroan dogtooth cement precipitated mainly in the moulds and not as much around grains. The ensuing cement stage corresponds to microsparitic ferroan geopetal cements (molar percentages of $FeCO_3$ from 0·59 to 0·65%) that formed in the meteoric vadose zone below a soil horizon (low $\delta^{13}C$) in reduced

conditions, and contemporaneously with the formation of an erosion surface (Figs 13B, 13C and 19). Microsparitic geopetal cements probably originated from the erosion of lithified substrates, producing a fine detritus that filtered downward forming geopetal internal sediment (Aissaoui & Purser, 1983). The erosion surface cross-cuts the micritic envelopes, the non-ferroan dogtooth cement and the ferroan microsparitic geopetal cements. The discontinuity surface was then flooded and covered by carbonate sediments. The last cement stage of composite surface 2 corresponds to brown-luminescent banded dogtooth cements both below and above the discontinuity. These cements precipitated in the phreatic meteoric zone, indicating a new emersion event that may have occurred during the formation of the next subaerial sequence boundary (Fig. 19).

CONCLUSIONS

For the first time, a total of 138 coupled $\delta^{13}C$ and $\delta^{18}O$ measurements were performed using a high-resolution ion microprobe spectrometer on blocky calcite cements, one telogenetic cement stage and 11 early cements and fabrics, along six key discontinuities from the Middle to Late Jurassic carbonates of the Paris Basin. The data allow for the precise tracing of the evolution of environmental conditions during the formation of discontinuities (pore water characteristics, redox conditions, presence of organic matter and microbial influence).

High-resolution variation of the $\delta^{13}C$ and $\delta^{18}O$ signals is measured within the same cement, which is not resolved with classical sampling methods such as microdrilling. This variability is well-illustrated within several millimetre-thick non-ferroan pendant cements, which display successive stages of crystallization in meteoric water, corresponding to dark-blue luminescent areas, and in marine to mixed water cements, characterized by narrow orange to pink-luminescent bands of fibrous crystals.

Micritic microbially induced fabrics such as meniscus-like cements and micritic envelopes precipitated directly as low-magnesium calcite in marine water in the Jurassic calcite sea, as attested to by the conservation of their initial marine $\delta^{18}O$ and very negative $\delta^{13}C$ signals. The high $\delta^{13}C$ values in the micritic fabrics vary between $-20{\cdot}0$ and $-0{\cdot}1‰$. The resin (polyepoxide) injected into the microporosity of micritic cements and fabrics could partially alter the $\delta^{13}C$ measurements, resulting in very negative $\delta^{13}C$ values (from $-14{\cdot}4$ to $-20{\cdot}0‰$).

Measurements in the current study also illustrate the variation of $\delta^{13}C$ and $\delta^{18}O$ signals for different cements which have the same morphology. Four types of dogtooth cements are identified, all with former low-magnesium mineralogy but each one having formed in a different environment. Ferroan or non-ferroan dogtooth cements formed in a subtidal environment, in reduced to oxidizing conditions, respectively. Brown-luminescent dogtooth cements grew in the meteoric phreatic zone from water with varying redox conditions that either percolated or not through an organic-rich soil horizon, resulting in a high variability of $\delta^{13}C$ signal from $-12{\cdot}7‰$ to $+6{\cdot}4‰$. Non-ferroan and non-isopachous dogtooth cements precipitated together with sparitic meniscus cements from meteoric water in the vadose oxidizing zone, below an organic-rich soil horizon in supratidal to continental environments.

The morphological and geochemical study of the early cement sequence below discontinuities allows the reconstruction of palaeoenvironmental events occurring during the sedimentary *hiatus* and thus the genetic history of the discontinuities. Five types of discontinuities are differentiated.

Subaerial exposure surface 1 displays pendant cements with a marine to meteoric $\delta^{18}O$ signal. The absence of Fe^{2+} indicates formation in the intertidal to supratidal domain, characterized by sporadic marine water inputs. Subaerial surface 2 presents meniscus cements associated with non-isopachous dogtooth cements that precipitated in the vadose meteoric zone under an organic-rich soil horizon. The third surface type is a marine hardground with fibrous isopachous cements and marine non-ferroan dogtooth cements, indicating precipitation in a subtidal environment in oxidizing water.

The last two surface types have a multiphase history. Composite surface 1 presents non-luminescent ferroan dogtooth and microsparitic bridge cements that precipitated in reducing conditions in eutrophic seawater, followed by brown-luminescent dogtooth cements characteristic of exposure. Composite surface 2 is marked by the development of microbially induced fabrics, formed in marine water with abundant organic matter. A subsequent increase in hydrodynamism, probably as the result of a relative sea-level fall, led to their partial erosion and to

the formation of geopetal peloidal fabrics. Hereafter, the discontinuity underwent emersion as attested to by the presence of ferroan geopetal cements. Brown-luminescent banded dogtooth cements formed during a later subaerial exposure stage because they are found within the sediments located both below and above the discontinuity.

This study shows that the integration of petrographic characterization and very high-resolution geochemical measurements is essential to deciphering subtle changes in environmental conditions during the formation of different discontinuities. This novel approach in the study of carbonate cements highlights a very high variability of $\delta^{18}O$ and especially $\delta^{13}C$ signatures within the same cement, whose amplitude can reach about 20‰ for the micritic fabrics. High-resolution ion microprobe study allows a precise characterization of the succession of events occurring during sedimentary gaps, which was not feasible using classical methods such as microdrilling. High-resolution geochemical analyses open perspectives for the development of new environmental models for discontinuity formation.

ACKNOWLEDGEMENTS

We are indebted to E. Deloule, M. Champenois, N. Bouden and A. Gurenkon for the use of the Cameca IMS-1280. We thank Michel Fiallin and Frédéric Couffignal for the use of the Cameca SXFive EPMA at the Centre CAMPARIS (Université Pierre et Marie Curie, Paris, France). We are grateful to Philippe Blanc (Lithologie Bourgogne) for the high-quality thin sections. This paper has benefited from discussions with C. Durlet and M. Pagel. The authors thank J.A.D. Dickson, Nicolas Christ and AE Christian Betzler for their constructive comments. This work resulted from collaborative project No PO4990 between University Paris-Sud and the BRGM. This project was funded by the BRGM and by a doctoral PhD from the French Ministry of Research and Higher Education (PhD grant No 2013-134).

REFERENCES

Aissaoui, D.M. and **Purser, B.H.** (1983) Nature and origins of internal sediment in Jurassic limestones of Burgundy (France) and Fnoud (Algeria). *Sedimentology*, **30**, 273–289.

Allison, N., **Finch, A.A.**, **Webster, J.M.** and **Clague, D.A.** (2007) Palaeoenvironmental records from fossil corals: the effects of submarine diagenesis on temperature and climate estimates. *Geochim. Cosmochim. Acta*, **71**, 4693–4703.

Andrieu, S., **Brigaud, B.**, **Rabourg, T.** and **Noret, A.** (2015) The Mid-Cenomanian event in shallow marine environments: influence on carbonate producers and depositional sequences (northern Aquitaine Basin, France). *Cretaceous Res.*, **56**, 587–607.

Andrieu, S., **Brigaud, B.**, **Barbarand, J.**, **Lasseur, E.** and **Saucède, T.** (2016) Disentangling the control of tectonics, eustasy, trophic conditions and climate on shallow-marine carbonate production during the Aalenian-Oxfordian interval: from the western France platform to the western Tethyan domain. *Sed. Geol.*, **345**, 54–84.

Ayalon, A., **Bar-Matthews, M.** and **Sass, E.** (1998) Rainfall-recharge relationships within a karstic terrain in the eastern Mediterranean semi-arid region, Israel: delta O-18 and delta D characteristics. *J. Hydrol.*, **207**, 18–31.

Bartley, J.K. (1996) Actualistic taphonomy of cyanobacteria: implications for the Precambrian fossil record. *Palaios*, **11**, 571–586.

Bates, N.R. and **Brand, U.** (1990) Secular variation of calcium carbonate mineralogy; an evaluation of ooid and micrite chemistries. *Geol. Rundsch.*, **79**, 27–46.

Bathurst, R.G.C. (1975) *Carbonate Sediments and Their Diagenesis*. Elsevier, Amsterdam, 658 pp.

Beddows, P.A., **Smart, P.L.**, **Whitaker, F.F.** and **Smith, S.L.** (2007) Decoupled fresh-saline groundwater circulation of a coastal carbonate aquifer: spatial patterns of temperature and specific electrical conductivity. *J. Hydrol.*, **346**, 18–32.

Boggs, S. and **Krinsley, D.** (2006) *Application of Cathodoluminescence Imaging to the Study of Sedimentary Rocks*. Cambridge University Press, Cambridge, 165 pp.

Brett, C.E. and **Brookfield, M.E.** (1984) Morphology, faunas and genesis of Ordovician hardgrounds from southern Ontario, Canada. *Palaeogeogr. Palaeoclimatol. Palaeoecol.*, **46**, 233–290.

Brigaud, B., **Pucéat, E.**, **Pellenard, P.**, **Vincent, B.** and **Joachimski, M.M.** (2008) Climatic fluctuations and seasonality during the Late Jurassic (Oxfordian-Early Kimmeridgian) inferred from $\delta^{18}O$ of Paris Basin oyster shells. *Earth Planet. Sci. Lett.*, **273**, 58–67.

Brigaud, B., **Durlet, C.**, **Deconinck, J.F.**, **Vincent, B.**, **Pucéat, E.**, **Thierry, J.** and **Trouiller, A.** (2009a) Facies and climate/environmental changes recorded on a carbonate ramp: a sedimentological and geochemical approach on Middle Jurassic carbonates. *Sed. Geol.*, **222**, 181–206.

Brigaud, B., **Durlet, C.**, **Deconinck, J.-F.**, **Vincent, B.**, **Thierry, J.** and **Trouiller, A.** (2009b) The origin and timing of multiphase cementation in carbonates: impact of regional scale geodynamic events on the Middle Jurassic limestones diagenesis (Paris Basin, France). *Sed. Geol.*, **222**, 161–180.

Brigaud, B., **Vincent, B.**, **Carpentier, C.**, **Robin, C.**, **Guillocheau, F.**, **Yven, B.** and **Huret, E.** (2014a) Growth and demise of the Jurassic carbonate platform in the intracratonic Paris Basin (France): Interplay of climate change, eustasy and tectonics. *Mar. Petrol. Geol.*, **63**, 3–29.

Brigaud, B., **Vincent, B.**, **Durlet, C.**, **Deconinck, J.-F.**, **Jobard, E.**, **Pickard, N.**, **Yven, B.** and **Landrein, P.** (2014b) Characterization and origin of permeability-porosity heterogeneity in shallow-marine carbonates: from core

scale to 3D reservoir dimension (Middle Jurassic, Paris Basin, France). *Mar. Petrol. Geol.*, **57**, 631–651.

Budd, D.A., **Hammes, U.** and **Ward, W.B.** (2000) Cathodoluminescence in calcite cements: new insights on Pb and Zn sensitizing, Mn activation, and Fe quenching at low trace-element concentrations. *J. Sed. Res.*, **70**, 217–226.

Carpentier, C., **Brigaud, B.**, **Blaise, T.**, **Vincent, B.**, **Durlet, C.**, **Boulvais, P.**, **Pagel, M.**, **Hibsch, C.**, **Yven, B.**, **Lach, P.**, **Cathelineau, M.**, **Boiron, M.-C.**, **Landrein, P.** and **Buschaert, S.** (2014) Impact of basin burial and exhumation on Jurassic carbonates diagenesis on both sides of a thick clay barrier (Paris Basin, NE France). *Mar. Petrol. Geol.*, **53**, 44–70.

Castanier, S. (1987) *Microbiogéologie: Processus et Modalités de la Carbonatogenèse Bactérienne*. PhD Thesis, Université de Nantes, France, 541 pp.

Castanier, S., **Le Métayer-Levrel, G.** and **Perthuisot, J.P.** (1997) Limestone genesis considered from the microbiogeologist point of view (abstract). IAS-ASF-IGCP 380 International Workshop on 'Microbial Mediation in Carbonate Diagenesis'. Chichilianne, Publication ASF, **26**, 13.

Castanier, S., **Le Métayer-Levrel, G.** and **Perthuisot, J.P.** (2000) Bacterial roles in the precipitation of carbonate minerals. In: *Microbial Sediments* (Eds R. Riding and M. Awramik), pp. 32–39. Springer Verlag, Heidelberg.

Catuneanu, O., **Galloway, W.E.**, **Kendall, C.G.S.C.**, **Miall, A.D.**, **Posamentier, H.W.**, **Strasser, A.** and **Tucker, M.** (2011) Sequence stratigraphy: methodology and nomenclature. *Newsl. Stratigr.*, **44**, 173–245.

Christ, N., **Immenhauser, A.**, **Amour, F.**, **Mutti, M.**, **Preston, R.**, **Whitaker, F.F.**, **Peterhänsel, A.**, **Egenhoff, S.O.**, **Dunn, P.A.** and **Agar, S.M.** (2012a) Triassic Latemar cycle tops – subaerial exposure of platform carbonates under tropical arid climate. *Sed. Geol.*, **265–266**, 1–29.

Christ, N., **Immenhauser, A.**, **Amour, F.**, **Mutti, M.**, **Tomàs, S.**, **Agar, S.M.**, **Always, R.** and **Kabiri, L.** (2012b) Characterization and interpretation of discontinuity surfaces in a Jurassic ramp setting (High Atlas, Morocco). *Sedimentology*, **59**, 249–290.

Christ, N., **Immenhauser, A.**, **Wood, R.**, **Darwich, K.** and **Niedermayr, A.** (2015) Petrography and environmental controls on the formation of Phanerozoic marine carbonate hardgrounds. *Earth-Sci. Rev.*, **151**, 176–226.

Clari, P.A., **Della Pierre, F.** and **Martire, L.** (1995) Discontinuities in carbonate successions: identification, interpretation and classification of some Italian examples. *Sed. Geol.*, **100**, 97–121.

Coimbra, R., **Immenhauser, A.** and **Olóriz, F.** (2009) Matrix micrite $\delta^{13}C$ and $\delta^{18}O$ reveals synsedimentary marine lithification in Upper Jurassic Ammonitico Rosso limestones (Betic Cordillera, SE Spain). *Sed. Geol.*, **219**, 332–348.

Cox, P.A., **Wood, R.A.**, **Dickson, J.A.D.**, **Al Rougha, H.B.**, **Shebl, H.** and **Corbett, P.W.M.** (2010) Dynamics of cementation in response to oil charge: evidence from a Cretaceous carbonate field, UAE. *Sed. Geol.*, **228**, 246–254.

Dera, G., **Brigaud, B.**, **Monna, F.**, **Laffont, R.**, **Puceat, E.**, **Deconinck, J.F.**, **Pellenard, P.**, **Joachimski, M.M.** and **Durlet, C.** (2011) Climatic ups and downs in a disturbed Jurassic world. *Geology*, **39**, 215–218.

Derry, L.A. (2010) A burial diagenesis origin for the Ediacaran Shuram-Wonoka carbon isotope anomaly. *Earth Planet. Sci. Lett.*, **294**, 152–162.

Dickson, J.A.D. (2002) Fossil echinoderms as monitor of the Mg/Ca ratio of Phanerozoic oceans. *Science*, **298**, 1222–1224.

Dickson, J.A.D. (2004) Echinoderm skeletal preservation: calcite-aragonite Seas and the Mg/Ca ratio of Phanerozoic oceans. *J. Sed. Res.*, **74**, 355–365.

Dickson, J.A.D. and **Kenter, J.A.M.** (2014) Diagenetic evolution of selected parasequences across a carbonate platform: Late Paleozoic, Tengiz reservoir, Kazakhstan. *J. Sed. Res.*, **84**, 664–693.

Dupraz, C., **Reid, R.P.**, **Braissant, O.**, **Decho, A.W.**, **Norman, R.S.** and **Visscher, P.T.** (2009) Processes of carbonate precipitation in modern microbial mats. *Earth-Sci. Rev.*, **96**, 141–162.

Durlet, C. and **Loreau, J.P.** (1996) Inherent diagenetic sequence of hardgrounds resulting from marine ablation of exposure surfaces. Example of the Burgundy platform, Bajocian (France). *CR Acad. Sci. Paris*, **323**, 389–396.

Durlet, C., **Loreau, J.P.** and **Pascal, A.** (1992) Signature diagénétique des discontinuités et nouvelle représentation graphique de la diagenèse. *CR Acad. Sci. Paris*, **314**, 1507–1514.

Ehrlich, H.L. (1996) *Geomicrobiology*, 3rd edn. Marcel Dekker, New York, 393 pp.

Enay, R. and **Mangold, C.** (1980) *Synthèse paléogéographique du Jurassique français. Document du Laboratoire de Géologie de Lyon*, Volume **5**. Groupe Français d'Etude du Jurassique, 220 pp.

Ferry, S., **Pellenard, P.**, **Collin, P.Y.**, **Thierry, J.**, **Marchand, D.**, **Deconinck, J.-F.**, **Robin, C.**, **Carpentier, C.**, **Durlet, C.** and **Curial, A.** (2007) Synthesis of recent stratigraphic data on Bathonian to Oxfordian deposits of the eastern Paris Basin. *Soc. Géol. Fr. Mém.*, **178**, 37–57.

Flügel, E. (2010) *Microfacies of Carbonate Rocks: Analysis, Interpretation and Implications*, 2nd edn. Springer-Verlag, Berlin, New York.

Folk, R.L. (1974) The natural history of crystalline calcium carbonate: effect of magnesium content and salinity. *J. Sed. Petrol.*, **44**, 40–53.

Gat, J.R., **Carmi, I.** and **Bauman, N.** (1994) The isotopic composition of precipitation at Bet-Dagan. Israel: the climatic record (1961–1990). *Israel Meteorol. Res. Pap.*, **5**, 10–19.

Godet, A., **Durlet, C.**, **Spangenberg, J.E.** and **Föllmi, K.B.** (2016) Estimating the impact of early diagenesis on isotope records in shallow-marine carbonates: a case study from the Urgonian Platform in western Swiss Jura. *Palaeogeogr. Palaeoclimatol. Palaeoecol.*, **454**, 125–138.

Guillocheau, F., **Robin, C.**, **Allemand, P.**, **Bourquin, S.**, **Brault, N.**, **Dromart, G.**, **Friedenberg, R.**, **Garcia, J.-P.**, **Gaulier, J.-M.**, **Gaumet, F.**, **Grosdoy, B.**, **Hanot, F.**, **le Strat, P.**, **Mettraux, M.**, **Nalpas, T.**, **Prija, C.**, **Rigollet, C.**, **Serrano, O.** and **Grandjean, G.** (2000) Meso-Cenozoic geodynamic evolution of the Paris Basin: 3D stratigraphic constraints. *Geodin. Acta*, **13**, 189–245.

Hamon, Y., **Merzeraud, G.** and **Combes, J.-P.** (2005) Des cycles de haute fréquence de variations du niveau marin relatif enregistrés dans les discontinuités sédimentaires : un exemple dans le Lias inférieur de Lodève (Sud-Est de la France). *Bull. Soc. Géol. Fr.*, **176**, 57–68.

Hendry, J.P. (2002) Geochemical trends and palaeohydrological significance of shallow burial calcite and ankerite cements in Middle Jurassic strata on the East Midlands Shelf (onshore UK). *Sed. Geol.*, **151**, 149–176.

Hendry, J.P., **Ditchfield, P.W.** and **Marshall, J.D.** (1995) Two-stage neomorphism of Jurassic aragonitic bivalves: implications for early diagenesis. *J. Sed. Res.*, **65**, 214–224.

Hillgärtner, H. (1998) Discontinuity surfaces on a shallow-marine carbonate platform (Berriasian, Valanginian, France and Switzerland). *J. Sed. Res.*, **68**, 1093–1108.

Hillgärtner, H., **Dupraz, C.** and **Hug, W.** (2001) Microbially induced cementation of carbonate sands: are micritic meniscus cements good indicators of vadose diagenesis? *Sedimentology*, **48**, 117–131.

IAEA (2000) *The Water Isotope System for data analysis, visualization and Electronic Retrieval (WISER) on the web site of the Global Network of Isotopes in Precipitation*, International Atomic Energy Agency, Vienna, Austria. Available at: www.iaea.org/water

Immenhauser, A., **Creusen, A.**, **Esteban, M.** and **Vonhof, H.B.** (2000) Recognition and interpretation of polygenic discontinuity surfaces in the Middle Cretaceous Shu'aiba, Nahr Umr, and Natih Formations of northern Oman. *GeoArabia*, **5**, 299–322.

Irwin, H., **Curtis, C.** and **Coleman, M.** (1977) Isotopic evidence for source of diagenetic carbonates formed during burial of organic-rich sediments. *Nature*, **29**, 209–213.

Kauffman, E.G., **Elder, W.P.** and **Sageman, B.B.** (1991) High-resolution correlation: a new tool in chronostratigraphy. In: *Cycles and Events in Stratigraphy* (Eds G. Einsele, W. Ricken and A. Seilacher), pp. 795–820. Springer, Berlin.

Kim, S.-T. and **O'Neil, J.R.** (1997) Equilibrium and nonequilibrium oxygen isotope effects in synthetic carbonates. *Geochim. Cosmochim. Acta*, **61**, 3461–3475.

Knoerich, A. and **Mutti, M.** (2003) Controls of facies and sediment composition on the diagenetic pathway of shallow-water heterozoan carbonates: the Oligocene of the Maltese Islands. *Int. J. Earth Sci.*, **92**, 494–510.

von Knorre, H. and **Krumbein, W.E.** (2000) Bacterial calcification. In: *Microbial Sediments* (Eds R. Riding and S.M. Awramik), pp. 25–31. Springer Verlag, Heidelberg.

Krumbein, W.E. (1979) Calcification by bacteria and algae. In: *Biogeochemical Cycling of Mineral-Forming Elements* (Eds P.A. Trudinger and D.J. Swaine), pp. 47–68. Elsevier, Amsterdam.

Lécuyer, C., **Picard, S.**, **Garcia, J.-P.**, **Sheppard, M.F.**, **Grandjean, P.** and **Dromart, G.** (2003) Thermal evolution of Tethyan surface waters during the Middle-Late Jurassic: evidence from $\delta^{18}O$ values of marine fish teeth. *Paleoceanography*, **18**, 1076.

Léonide, P., **Floquet, M.**, **Durlet, C.**, **Baudin, F.**, **Pittet, B.** and **Lécuyer, C.** (2012) Drowning of carbonate platform as a precursor stage of the Early Toarcian global anoxic event (Southern Provence sub-Basin, South-east France). *Sedimentology*, **59**, 156–184.

Longman, M.W. (1980) Carbonate diagenetic textures from nearsurface diagenetic environments. *AAPG Bull.*, **64**, 461–487.

Loreau, J.P. and **Durlet, C.** (1999) Diagenetic stratigraphy of discontinuity surfaces: an application to paleo-environments and sequence stratigraphy. *Zbl. Geol. Paläontol.*, **1**, 381–407.

Machel, H.G. (1985) Cathodoluminescence in calcite and dolomite and its chemical interpretation. *Geosci. Can.*, **12**, 139–147.

Machel, H.G. (2000) Application of cathodoluminescence to carbonate diagenesis. In: *Cathodoluminescence in Geosciences* (Eds M. Pagel, V. Barbin, P. Blanc and D. Ohnenstetter), pp. 303–329. Springer-Verlag, Berlin.

Machel, H.G., **Mason, R.A.**, **Mariano, A.N.** and **Mucci, A.** (1991) Causes and emission of luminescence in calcite and dolomite. In: *Luminescence Microscopy and Spectroscopy: Qualitative and Quantitative Applications* (Eds C.E. Barker and O.C. Kopp), *SEPM Short Course*, **25**, 9–25.

Major, R.P. (1991) Cathodoluminescence in Post-Miocene carbonates. In: *Luminescence Microscopy and Spectroscopy: Qualitative and Quantitative Applications* (Eds C.E. Barker and O.C. Kopp), *SEPM Short Course*, **25**, 149–153.

Mallarino, G., **Goldstein, R.H.** and **Di Stefano, P.** (2002) New approach for quantifying water depth applied to the enigma of drowning of carbonate platforms. *Geology*, **30**, 783–786.

Martinez, M. and **Dera, G.** (2015) Orbital pacing of carbon fluxes by a ~9-My eccentricity cycle during the Mesozoic. *Proc. Natl Acad. Sci. USA*, **112**, 12604–12609.

Martinuš, M., **Bucković, D.** and **Kukoć, D.** (2012) Discontinuity surfaces recorded in shallow-marine platform carbonates: an example from the Early Jurassic of the Velebit Mt. (Croatia). *Facies*, **58**, 649–669.

Moguedet, G., **Charnet, F.**, **Gresselin, F.** and **Lemoine, B.** (1998) *Notice explicative de la carte géologique de Mortagne-au -Perche (1/50000)*. Éditions du BRGM, 87 pp.

Morse, J.W. and **Mackenzie, F.T.** (1990) *Geochemistry of Sedimentary Carbonates. Developments in Sedimentology 48*. Elsevier, Amsterdam, 707 pp.

Nader, F.H., **Champenois, F.**, **Barbier, M.**, **Adelinet, M.**, **Rosenberg, E.**, **Houel, P.**, **Delmas, J.** and **Swennen, R.** (2016) Diagenetic effects of compaction on reservoir properties: the case of early Callovian "Dalle Nacrée" formation (Paris Basin, France). *J. Geodynamics*, **101**, 5–29.

Navarro-Ramirez, J.P., **Bodin, S.** and **Immenhauser, A.** (2015) Ongoing Cenomanian - Turonian heterozoan carbonate production in the neritic settings of Peru. *Sed. Geol.*, **331**, 78–93.

Pagel, M., **Barbarand, J.**, **Beaufort, D.**, **Gautheron, C.** and **Pironon, J.** (2014) *Bassins sédimentaires - les marqueurs de leur histoire thermique*. Edp science, Société Géologique de France, 228 pp.

Palmer, T.J., **Hudson, J.D.** and **Wilson, M.A.** (1988) Palaeoecological evidence for early aragonite dissolution in ancient seas. *Nature*, **335**, 809–810.

Purser, B.H. (1969) Syn-sedimentary marine lithification of Middle Jurassic in the Paris Basin. *Sedimentology*, **12**, 205–230.

Richter, D.K., **Götte, T.**, **Götze, J.** and **Neuser, R.D.** (2003) Progress in application of cathodoluminescence (CL) in sedimentary petrology. *Mineral. Petrol.*, **79**, 127–166.

Riding, R. (2000) Microbial carbonates: the geological record of calcified bacterial–algal mats and biofilms. *Sedimentology*, **47**(s1), 179–214.

Rioult, M., **Coutard, J.-P.**, **Helluin, M.**, **Larsonneur, C.** and **Pellerin, J.** (1989) *Notice explicative de la carte géologique de Caen* (1/50000). Éditions du BRGM, 104 pp.

Rioult, M., **Dugué, O.**, **Jan du Chêne, R.**, **Ponsot, C.**, **Fily, G.**, **Moron, J.M.** and **Vail, P.R.** (1991) Outcrop sequence stratigraphy of the Anglo-Paris Basin Middle to Upper Jurassic (Normandy, Maine, Dorset). *Bull. Centres Rech. Explor.-Prod. Elf-Aquitaine*, **15**, 1–194.

Rollion-Bard, C., **Blamart, D.**, **Cuif, J.P.** and **Juillet-Leclerc, A.** (2003) Microanalysis of C and O isotopes of azooxanthellate and zooxanthellate corals by ion microprobe. *Coral Reefs*, **22**, 405–415.

Rollion-Bard, C., **Mangin, D.** and **Champenois, M.** (2007) Development and applications of oxygen and carbon isotopic measurements of biogenic carbonates by ion microprobe. *Geostandards Geoanalytical Res.*, **31**, 39–50.

Rollion-Bard, C., **Erez, J.** and **Zilberman, T.** (2008) Intra-shell oxygen isotope ratios in the benthic foraminifera genus *Amphistegina* and the influence of seawater carbonate chemistry and temperature on this ratio. *Geochim. Cosmochim. Acta*, **72**, 6006–6014.

Ronchi, P., **Ortenzi, A.**, **Borromeo, O.**, **Claps, M.** and **Zempolich, W.G.** (2010) Depositional setting and diagenetic processes and their impact on the reservoir quality in the late Visean-Bashkirian Kashagan carbonate platform (Pre-Caspian Basin, Kazakhstan). *AAPG Bull.*, **94**, 1313–1348.

Sandberg, P.A. (1983) An oscillating trend in Phanerozoic non-skeletal carbonate mineralogy. *Nature*, **305**, 19–22.

Sattler, U., **Immenhauser, A.**, **Hillgärtner, H.** and **Esteban, M.** (2005) Characterization, lateral variability and lateral extent of discontinuity surfaces on a carbonate platform (Barremian to Lower Aptian, Oman). *Sedimentology*, **52**, 339–361.

Schubert, B.A. and **Jahren, A.H.** (2015) Seasonal temperature and precipitation recorded in the intra-annual oxygen isotope pattern of meteoric water and tree-ring cellulose. *Quatern. Sci. Rev.*, **125**, 1–14.

Strasser, A., **Pittet, B.** and **Wolfgang, H.** (2015) Palaeogeography of a shallow carbonate platform: the case of the Middle to Late Oxfordian in the Swiss Jura Mountains. *J. Palaeogeogr.*, **4**, 251–268.

Thierry, J. and **Barrier, E.** (2000) Late sinemurian, middle toarcian, middle callovian, early kimmeridgian, early tithonian. In: *Atlas Peri-Tethys, Palaeogeographical Maps–Explanatory Notes* (Ed. S. Crasquin) pp. 49–110. CCGM/CGMW Edit, Paris.

Tobin, K.J., **Walker, K.R.**, **Steinhauff, D.M.** and **Mora, C.I.** (1996) Fibrous calcite from the Ordovician of Tennessee: preservation of marine oxygen isotopic composition and its implications. *Sedimentology*, **43**, 235–251.

Turpin, M., **Gressier, V.**, **Bahamonde, J.R.** and **Immenhauser, A.** (2014) Component-specific petrographic and geochemical characterization of fine-grained carbonates along Carboniferous and Jurassic platform-to-basin transects. *Sed. Geol.*, **300**, 62–85.

Videtich, P.E. and **Matthews, R.K.** (1980) Origin of discontinuity surfaces in limestones: isotopic and petrographic data, Pleistocene of Barbados, west Indies. *J. Sed. Petrol.*, **50**, 971–980.

Vincent, B., **van Buchem, F.S.**, **Bulot, L.G.**, **Jalali, M.**, **Swennen, R.**, **Hosseini, A.S.** and **Baghbani, D.** (2015) Depositional sequences, diagenesis and structural control of the Albian to Turonian carbonate platform systems in coastal Fars (SW Iran). *Mar. Petrol. Geol.*, **63**, 46–67.

Visscher, P.T., **Prins, R.A.** and **van Gemerden, H.** (1992) Rates of sulfate reduction and thiosulfate consumption in a marine microbial mat. *FEMS Microbiol. Ecol.*, **86**, 283–294.

Volery, C., **Davaud, E.**, **Foubert, A.** and **Caline, B.** (2009) Shallow-marine microporous carbonate reservoir rocks in the Middle East: relationship with seawater Mg/Ca ratio and eustatic sea level. *J. Petrol. Geol.*, **32**, 313–325.

Volery, C., **Davaud, E.**, **Foubert, A.** and **Caline, B.** (2010a) Lacustrine microporous micrites of the Madrid Basin (Late Miocene, Spain) as analogues for shallow-marine carbonates of the Mishrif reservoir Formation (Cenomanian to Early Turonian, Middle East). *Facies*, **56**, 385–397.

Volery, C., **Davaud, E.**, **Durlet, C.**, **Clavel, B.**, **Charollais, J.** and **Caline, B.** (2010b) Microporous and tight limestones in the Urgonian Formation (Late Hauterivian to Early Aptian) of the French Jura Mountains: focus on the factors controlling the formation of microporous facies. *Sed. Geol.*, **230**, 21–34.

Volery, C., **Suvorova, E.**, **Buffat, P.**, **Davaud, E.** and **Caline, B.** (2011) TEM study of Mg distribution in micrite crystals from the Mishrif reservoir Formation (Middle East, Cenomanian to Early Turonian). *Facies*, **57**, 605–612.

Wilkinson, B.H. and **Algeo, T.J.** (1989) Sedimentary carbonate record of calcium magnesium cycling. *Am. J. Sci.*, **289**, 1158–1194.

Wilkinson, B.H., **Smith, A.L.** and **Kyger, C.L.** (1985) Sparry calcite marine cement in Upper Jurassic limestones of southeastern Wyoming. In: *Carbonate Cements* (Eds N. Schneidermann and P.M. Harris), *SEPM Spec. Publ.*, **36**, 169–184.

Zheng, Y.F. (1999) Oxygen isotope fractionation in carbonate and sulfate minerals. *Geochemical J.*, **33**, 109–126.

Ziegler, P.-A. (1988) Evolution of the Arctic - North Atlantic and the Western Tethys. *AAPG Mem.*, **43**, 164–196.

Manuscript received 7 November 2016; revision accepted 4 May 2017